Title
Evaporation and Molecular Beam Scattering from a Flat Liquid Jet

Journal
The Journal of Physical Chemistry A, 126(21)

ISSN
1089-5639

Authors
Lee, Chin
Pohl, Marvin N
Ramphal, Isaac A
et al.

Publication Date
2022-06-02

DOI
10.1021/acs.jpca.2c01174

Peer reviewed

Evaporation and molecular beam scattering from a flat liquid jet

Chin Lee,‡ *Marvin N. Pohl,*‡ *Isaac A. Ramphal, Walt Yang, Bernd Winter, Bernd Abel,*

*Daniel M. Neumark**

ABSTRACT

An experimental setup for molecular beam scattering from flat liquid sheets has been developed, with the goal of studying reactions at gas-liquid interfaces for volatile liquids. Specifically, a crossed molecular beam instrument that can measure angular and translational energy distributions of scattered products has been adapted for liquid jet scattering. A microfluidic chip is used to create a stable flat liquid sheet inside vacuum from which scattering occurs, and both evaporation and scattering from this sheet are characterized by a rotatable mass spectrometer that can measure product time-of-flight distributions. This manuscript describes the instrument and reports on first measurements of evaporation of dodecane and Ne from a Ne-doped dodecane flat jet, as well as scattering of Ne from a flat jet of pure dodecane.

1. INTRODUCTION

The gas-liquid interface is a ubiquitous chemical environment in nature. It plays a major role in industrial processes, atmospheric chemistry, and environmental science. Examples include air-fuel mixing in internal combustion engines,[1] acid rain formation,[2-4] tropospheric aerosol surface chemistry, [5] and the uptake of CO_2 at the ocean-air interface, where about one third of anthropogenically generated CO_2 is absorbed.[6] It is thus desirable to develop a molecular-scale understanding of chemistry at the gas-liquid interface.

Experiments employing an array of techniques have demonstrated that chemistry at the interface of a liquid solution can differ markedly from that in a bulk liquid or in the gas phase.[7-9] As examples, second harmonic and sum-frequency generation that rely on symmetry-breaking effects at the surface provide highly surface-specific spectroscopic information on species at the liquid interface.[10-12] X-ray photoelectron spectroscopy of liquid jets[13-16] and aerosols[17] probes solvent and solute molecules lying within 1-3 nm of the interface. Surface-sampling of Langmuir troughs enables chemical analysis of photochemical products at the liquid interface and in the bulk.[18] Mass spectrometry-based experiments

on thin films as well as droplets in microemulsions and the gas phase have shown significantly enhanced surface chemical reaction rates compared to bulk liquids.[19-21]

Molecular beam scattering, originally developed to probe interactions between pairs of gas-phase molecules[22, 23] and gas-phase molecules with solid surfaces,[24, 25] has proved to be a direct and powerful means for investigating the dynamics of elementary chemical reactions. Nathanson and others have shown that molecular beam scattering from liquids offers a unique probe of gas-liquid interfacial interactions.[26] Through this technique, two possible mechanisms are revealed – impulsive scattering (IS) and thermal desorption (TD). These mechanisms give rise to components with fast and slow velocity distributions, respectively. The TD signal represents gas molecules that undergo surface-trapping upon impact with the liquid surface long enough for thermalization to occur prior to desorption. IS results from gas molecules that do not penetrate the liquid and experience negligible surface-residence times (with respect to thermalization), recoiling elastically or losing only a fraction of their initial energy. They scatter preferentially into angles that depend sensitively on initial energy and impact angle.[27]

Molecular beam surface scattering experiments require compatibility with a vacuum environment and a clean sample surface, both of which are particularly challenging for liquid samples. Great advances were made by Fenn and coworkers developing a robust technique that utilized spinning wheels to generate

continuously refreshed liquid films.[28, 29] This "wetted wheel" approach was later used by Nathanson, Minton, and others to perform molecular scattering experiments at low vapor pressure systems (< 10^{-3} Torr) including long-chain hydrocarbons,[30] glycerol,[31] ionic liquids,[32] salty water at 212 K,[33] and perfluoropolyether.[34]

In order to carry out experiments on more volatile liquids, Faubel and coworkers developed micrometer-thin cylindrical water jets.[35, 36] They showed that the small size and curvature of these jets greatly lowers the vapor density above the surface, thus reducing gas-phase collisions between evaporating particles. In 2013, Nathanson used the liquid jet technique for gas-liquid scattering experiments,[37] and was able to study molecular beam scattering from liquid water and other volatile liquids. These included collisions of DCl molecules with salty water at 238 K,[38] scattering of Ne and O_2 from liquid dodecane,[37] collisions of Cl_2 and N_2O_5 with surfactant-coated Br^--glycerol solutions,[39, 40] and organic molecule collisions with salty water.[41]

Despite the access to higher vapor pressure liquids provided by the cylindrical microjet, its geometry is not particularly well-suited for scattering experiments. A cylindrical jet provides a much smaller scattering target than a wetted wheel; its typical diameter of 15-30 μm is considerably smaller than the usual dimensions of molecular beams (~1 mm). Moreover, the scattering angle from a cylindrical jet is not

well-defined, making it challenging to measure product angular distributions, a central attribute of scattering experiments.

We herein present a novel approach of producing mm^2-sized flat liquid sheets inside vacuum to facilitate gas-liquid scattering experiments with a more optimal scattering target. These so-called "flat jets" have been successfully used in various spectroscopy experiments.[42-46] The goal of this work is to extend the capabilities of scattering experiments to the surfaces of volatile liquid flat jets, enabling both the speed and angular distributions of escaping molecules to be determined. As such, the current work presents the first application of flat liquid jets in a scattering experiment. We focus here on the volatile liquid dodecane, a key component of jet fuel surrogates,[47] to present current experimental capabilities.

Two types of experiments are carried out: evaporation and scattering. We explore evaporation of Ne-doped dodecane solutions in order to isolate the trapping-desorption process, which is one of the major channels encountered in scattering experiments, and a detailed understanding of evaporation from a flat jet will be key to successfully interpreting scattering experiments. Additionally, evaporation provides the opportunity to explore the performance of our instrument as liquid evaporation from cylindrical jets has been extensively studied.[37] Molecular beam scattering experiments of Ne from a dodecane flat jet are also

described, in which measurement of the scattered Ne velocity and angular distributions enables elucidation of the IS and TD mechanisms.

2. EXPERIMENTAL

2.1 Instrument Design

The gas-liquid scattering apparatus consists of a modified crossed molecular beam machine described elsewhere in great detail.[48, 49] The general layout is shown in Fig. 1(a). It consists of a source chamber where a molecular beam is produced, a main chamber where the beam interacts with the liquid jet, and a detector chamber that houses the ionization and detection components. All chambers are pumped by turbomolecular pumps. In the source chamber, a pulsed molecular beam is generated using a piezoelectric valve (MassSpecpecD BV, Enschede) operated at a 200 Hz repetition rate and a pulse duration of 20-30 μs (FWHM, measured 330 mm downstream from the valve orifice).[50, 51] Stagnation conditions within the valve reservoir are typically 286 K and 3000 Torr, leading to supersonic expansion of the gas mix through a 500 μm orifice when the valve is opened. The beam expands for 40 mm before encountering a 1 mm diameter conical skimmer that separates the source and main chambers. After another 30 mm the molecular beam passes through a second 1 mm collimation skimmer. Residual transverse velocity in the molecular beam leads to a beam size of 4 mm at the interaction region. With a flat jet width of around

1 mm (see next section), some portion of the beam will miss the jet and can pass directly into the detector. This effect is most pronounced within 5° of the molecular beam axis (x-axis in Fig. 1(a) and 1(b)), thus we typically position the detector at least 20° from the beam axis to eliminate this contribution.

The main chamber is where the gas-liquid interactions take place. Using translation mechanisms described below, a liquid jet is precisely positioned at the interaction region where the molecular beam and detector fields of view intersect. The detector chamber is housed within the main chamber and comprises an electron impact ionizer, quadrupole mass filter, and ion detector components.[48] It consists of three differentially pumped regions and can be sealed from the main chamber by a gate valve, which opens to either a 100 μm diameter circular aperture or a 3 × 3 mm^2 square aperture. The small aperture is used for molecular beam velocity characterization while the larger aperture is used for evaporation and scattering experiments in order to view the entire width of the flat jet.

Typical pressures in the main chamber range in the low to mid 10^{-6} Torr range depending on whether a dodecane jet is running or not. This low main chamber pressure during jet operation is achieved by installing a large copper panel cooled by a gravity-fed liquid nitrogen dewar. This cryogenic shield has an area of approximately 0.98 m^2. With a sticking coefficient for dodecane of essentially unity, similar to water, the pumping speed is estimated as ~45,000 L s^{-1}.[52] The pressure reduction observed with the

cryogenic shield is consistent with this factor of increase in pumping speed. The ionizer chamber pressure is in the low to mid 10^{-11} Torr range, achieved by a combination of three stages of differential pumping (regions RI-RIII) and liquid nitrogen cryogenic cooling.

The liquid jet must be aligned simultaneously with respect to a catcher that disposes the liquid waste and to the molecular beam and detector axes.[53] This is achieved by an array of piezoelectric stages that allow for independent control over the three translational dimensions of the catcher relative to the jet, as well as the entire jet-catcher assembly relative to the interaction region. The setup is shown in Fig. 1(b). The entire jet assembly is mounted on a precise stepper motor that can retract both the jet and catcher several centimeters away from the molecular beam axis, allowing direct characterization of the molecular beam prior to scattering experiments. In addition, the jet holder is mounted to a 360˚ rotation stage in order to vary the molecular beam incident angle, θ_i. The positions of the jet and catcher are monitored using two cameras equipped with zoom lenses.

For evaporation experiments, the molecular beam is shut off and the liquid surface is positioned such that the surface normal (y-axis in Fig. 1(a) and 1(b)) is perpendicular to the molecular beam axis. In this configuration the detector can sweep through 0^o to 90˚ with respect to the jet surface normal. For scattering

experiments, the molecular beam is directed onto the liquid surface. While θ_i can be freely chosen, we are limited to detector positions for the scattering angles, θ_f, between 90° - θ_i and 90°.

2.2 Liquid Jet Generation

Experiments have previously been carried out on flat jets formed by colliding two individual cylindrical jets,[42, 44, 54, 55] but space limitations around the interaction region in our setup necessitate a more compact approach. The nozzle design routinely used in our lab is a microfluidic chip made by etching channels into borosilicate glass, developed by Micronit BV in collaboration with SLAC National Accelerator Laboratory.[56] As shown in Fig. 1(c), the chip has three channels, where the central channel is connected to one inlet port, along with another inlet port that diverges into two outer channels that then re-converge at the nozzle exit. The central channel and outer channels have dimensions of $20 \times 25\ \mu m^2$ and $50 \times 55\ \mu m^2$, respectively, with a 5 μm tolerance for each dimension. This nozzle was designed to operate as a gas dynamic virtual nozzle at SLAC, using high-pressure gas in the outer channels to compress liquid from the central channel into extremely thin sheets (< 20 nm). Gas dynamic jet operation is obviously not compatible with a molecular scattering experiment. Instead, during operation in colliding jet mode, liquid is pumped through the outer channels while the inner channel is left unused. Cylindrical jet operation is possible by swapping the liquid inlet from the split outer channels to the single central channel. The dimensions of this channel lead to a cylindrical jet approximately 25 μm in diameter. Fig. 1(d) shows a

dodecane flat jet produced using this nozzle design with the colliding jet mode by pumping 2.5 mL min^{-1} of dodecane into the split outer channels.

Liquid is delivered to the jet nozzle through 1/16-inch PEEK tubing lines and pressurized using a high-performance liquid chromatography (HPLC) pump at flow rates between 0.5-3.5 mL min^{-1}, resulting in pressures between 10-70 bar depending on the in-line particulate filter pore size, jet nozzle, and liquid viscosity (determined by the liquid temperature and solvent identity). This translates to flow velocities between 2-12 m s^{-1}, which means that particles that stick onto the liquid surface must desorb within about 1-10 ms before they are carried out of view of the detector. The fixed 80° collision angle of these commercially available nozzles conveniently produces jets with dimensions compatible with molecular beams. Typical dimensions are 1.7 × 5.1 mm^2 (W × H) flat sheets for dodecane at 3.5 mL min^{-1} flow rate, bounded by a thicker fluid rim with diameter around 50 μm.[56] Before reaching the jet nozzle, the liquid passes through a counter-current heat-exchanger to lower its temperature and thus reduce the vapor pressure of the liquid. The coolant in the heat-exchanger is set to be close to the liquid's freezing point; for example, it is set to -7 ℃ for dodecane for which the freezing point is -9 ℃. This heat exchanger is attached to the chamber such that its exit side is inside the vacuum and therefore minimizes possible heat transfer en route to the nozzle.

Often, cylindrical liquid jets in vacuum are collected by directing them onto a cryogenically cooled surface that freezes the liquid waste and stores it inside the vacuum chamber.[46, 57] However, when using a flat jet with much higher flow rates, it is preferable to catch the jet 2-5 mm downstream with a small orifice placed at the sheet node.[42, 53] Thus, only a small fraction of the jet is exposed to the vacuum, which drastically reduces the overall gas load in the chamber. We use a stainless-steel catcher with a 1 mm diameter orifice to collect the liquid jet. We have the additional capability to collect more volatile solvents in the future by installing a heated copper-beryllium catcher by Microliquids GmbH (defunct, similar in design to the catcher made by Advanced Microfluidic Systems GmbH, Göttingen). The bottom of the catcher is connected to a flexible 1/4-inch Teflon hose which drains liquid out of the main chamber and into a collection bottle for recycling. This bottle sits in an ice-bath and is pumped by a mechanical pump in series with a 4 L liquid nitrogen-cooled foreline trap. The collection reservoir pressure is maintained at $\sim 10^{-3}$ Torr under most conditions.

2.3 Experimental Protocol

Velocities of the molecular beams are determined by time-of-flight (TOF) measurements, using a rotating disk spinning at 200 Hz and containing two narrow slits (16 μs opening) to "chop" a narrow section of the most intense part of the beam. The flight time is measured from the chopper disk to the

detector for evaporation experiments, while for scattering experiments time zero occurs when the most intense part of the molecular beam reaches the interaction region.

Angular distributions from the flat jet were measured from integrated TOF spectra collected at angles between 0˚ (parallel to the jet normal) and 90˚ (parallel to the jet surface) in a back-and-forth manner over four rounds in order to monitor long-term signal instabilities. For each round, the 0˚ TOF spectrum was measured as a reference, and signal intensities at other angles were normalized accordingly. Overall signal intensities, however, were observed to be rather stable with a standard deviation of 3 and 5% for the five 0˚ spectra of dodecane and Ne evaporation. Total acquisition times and ionizer emission currents differ between spectra as we always aimed to achieve good signal-to-noise ratios (S/N) while minimizing the accumulation time and preventing detector saturation. Typical values are 5-15 min acquisition time per spectrum at ionizer emission currents ranging from 0.5-3.8 mA.

In the evaporation experiments, neon (99.99% purity) is dissolved in dodecane (n-$C_{12}H_{26}$, TCI America #D0968) by vacuum-degassing the liquid. The degassing process is carried out by simultaneously sonicating and pumping the liquid reservoir with a mechanical pump for 10 min followed by bubbling noble gas through the liquid until the bottle is pressurized to atmospheric pressure. This procedure was typically repeated five times. We selected Ne atoms as the solute as they are inert and have no internal

degrees of freedom, which reduces the solute-surface and solute-vapor interactions to physical mechanisms. Moreover, the mass of Ne does not overlap with any solvent ionization fragments produced from dodecane. Dodecane was detected at $m/z = 57$ ($C_4H_9^+$), which represents the butyl cation, a dissociative ionization fragment of dodecane seen at a higher signal intensity than the parent ion ($m/z = 170$, $C_{12}H_{26}^+$).[58]

For the scattering experiments, we used pure dodecane flat jets. We produced molecular beams with velocities of 789 ± 44 m s^{-1} and 1450 ± 51 m s^{-1} (FWHM) for "slow" Ne (pure) and "fast" Ne (seeded in a 1:9 ratio in He), respectively. The mean translational energies of the incident beam are 6.3 and 21.2 kJ mol^{-1}, respectively. The temporal beam widths are measured to be 65 and 26 μs (FWHM) for slow and fast Ne beams. In these experiments, θ_i is chosen to be 45˚, 60˚ or 80˚. TOF spectra are taken without a post-scattering chopper; hence scattering from the full incident beam profile is collected, but the temporal resolution of the measurement is limited by the duration of the pulsed beam. During data collection for scattering experiments, the background signal in the vacuum chamber is excluded by subtracting "beam-off" from "beam-on" data.

The flat jet is always caught by a catcher at its first node and therefore only the first liquid sheet is exposed (see Fig. 1(c)). A thermocouple is attached onto the stainless-steel chip holder (see Fig. 1(b)) to

estimate the liquid temperature inside the holder T_{holder}, which we assume to be equal to the liquid at the chip outlet. The liquid temperature reported in this paper T_{liq} is defined as the jet temperature at the detector axis, which is typically 1.5 mm downstream from the tip of the chip for the cylindrical jets and 2 mm downstream for the flat jet. While the cylindrical jet T_{liq} is calculated using the jet temperature equation,[59, 60] the flat jet T_{liq} is estimated by using the cylindrical jet temperature equation augmented by an extra term that approximates the ratio of perimeter to sectional area, in order to compensate for the increased evaporative cooling of the flat jet. We estimate the temperature drop T_{holder} - T_{liq}, caused by evaporative cooling, to be less than 0.5 ℃ in our experiment due to the low vapor pressure of dodecane ($P_{vap} = 1.5 \times 10^{-2}$ Torr at 275 K).[61]

3. EXPERIMENTAL RESULTS AND ANALYSIS

3.1 Evaporation

TOF spectra of dodecane and Ne evaporating from flat jets of Ne-doped liquid dodecane are presented in Fig. 2 and compared to evaporation from cylindrical jets. The detector angle θ_f is defined in Fig. 3(a). Jet temperatures ranged between T_{liq} = 268 and 291 K, and are indicated for each spectrum in the figure caption. Angular distributions for dodecane and Ne evaporating from the flat jet are shown in Fig. 3(b) and will be discussed below.

Dodecane evaporation data from a cylindrical jet (Fig. 2(a), bottom trace) is almost perfectly fit by a Maxwell-Boltzmann (MB) distribution (blue trace) corresponding to the measured liquid temperature with only a small deviation at longer flight times. The fit indicates that liquid molecules are fully thermalized with the surface liquid when they evaporate. This scenario is identical to the desorption step of the TD scattering mechanism assuming complete thermalization occurs. The MB flux distribution is given by: [62]

$$f_{\mathrm{MB}}(v) \propto v^3 \exp\left(-\frac{mv^2}{2RT_{liq}}\right) \quad (1)$$

where v and m are the velocity and molecular mass of the evaporating molecule, R is the universal gas constant and T_{liq} is the liquid temperature.

Dodecane evaporation from the flat jet is shown in the upper traces in Fig. 2(a) for detector angles θ_{f} of 0˚, 30˚, 60˚ and 90˚. The 90˚ TOF spectrum, which essentially reflects evaporation from the ~50 μm thick jet rims, strongly resembles the MB distribution of the 25-μm cylindrical jet. We estimate that evaporation from the rims contributes < 3% to the total flux and is thus negligible at large angles. With decreasing θ_{f}, the TOF spectra shift towards faster arrival times and become narrower than what is anticipated for MB evaporation at T_{liq} – the spectra indicate a super-Maxwellian velocity distribution. For dodecane at 0˚, the TOF spectrum deviates most significantly from the MB distribution. We also observe a narrowing in our Ne TOF spectra in Fig. 2(b) with decreasing θ_{f}. However, here the MB distribution at T_{liq} agrees better

with the 0˚ TOF spectrum, while the 90˚ spectrum has a noticeably slower and broadened shape. It thus appears that the angle-dependent deviations from a MB distribution in dodecane and Ne evaporation arise from different effects.

We first investigate the super-Maxwellian effect in dodecane evaporation. This phenomenon can be explained by the effect of vapor-phase collisions between evaporating particles above the jet surface that result in acceleration in a manner analogous to supersonic molecular beam formation.[36] Under these conditions, it is expected that the data will be well simulated by the flux expression for a supersonic (SS) molecular beam with average flow velocity v_{SS} and average temperature T_{SS}:[63, 64]

$$f_{SS}(v) \propto v^3 \exp\left(-\frac{m(v-v_{SS})^2}{2RT_{SS}}\right). \qquad (2)$$

In the limit of zero collisions, no conversion of thermal motion to flow velocity will occur ($v_{SS} = 0$ and $T_{SS} = T_{liq}$), and $f_{SS}(v)$ becomes the MB distribution $f_{MB}(v)$ shown in Eq. 1. The data in Fig. 2(a) are fit very well by Eq. 2 (red traces) for both flat and cylindrical jets. A plot of the fit parameters is presented in Fig. 4, where the cylindrical jet data is fit with v_{SS} = 73 m s^{-1} and T_{SS} = 210 K (open circle and square). These values deviate slightly from those for a MB distribution ($v_{SS} = 0$ and $T_{SS} = T_{liq}$ = 289 K), suggesting some collisions occur between the evaporating molecules. In contrast, the flat jet parameters exhibit a considerably larger deviation from the MB distribution. We find that v_{SS} increases from 90 to 135 m s^{-1}

with decreasing θ_f, accompanied by a decrease in T_{SS}. Hence, there is considerable thermal relaxation analogous to a supersonic beam expansion which is most prominent at low θ_f.

The evolution of super-Maxwellian to Maxwellian distributions from $\theta_f = 0^\circ$ to 90° can be understood by the vapor cloud density around the jet. A higher vapor pressure leads to a shorter mean free path λ and therefore a higher collision number N_{coll} for molecules exiting the liquid surface before reaching the detector. One way to describe the trend of N_{coll} is by the cosine law of evaporation,[65, 66] which states that the directional distribution of the evaporating molecules from a flat surface follows a $\cos\theta_f$ distribution, so that there are more collisions at angles closer to the surface normal. Another way to estimate N_{coll} is by using an electrostatic analogy,[60] where electric field corresponds to pressure and electric potential, the integral of the electric field, is analogous to N_{coll}. For example, a flat jet is often simulated by a uniformly charged disk electrode and a cylindrical jet by a charged cylinder. Based on this picture, the evaporative flux decreases with increasing θ_f, similar to how the electric field around a finite disk distorts towards the edges.[67, 68]

To lower N_{coll} it is necessary to increase λ, which is inversely proportional to the vapor density and collision cross section σ. The vapor density is a function of liquid temperature and is limited by the freezing point. However, σ can be reduced by the choice of particles involved. The dodecane-dodecane

hard-sphere cross section has previously been estimated to be ~250 Å^2,[37, 69] and is roughly two times smaller for Ne-dodecane. In fact, the relative Ne-dodecane cross section should be even smaller given the omission of van der Waals interactions in the above estimation and considering the very weak interactions between Ne and other species.

In contrast to dodecane evaporation, the TOF spectrum of Ne evaporation at $\theta_f = 0°$ is very well fit by a MB distribution. Moreover, Ne exhibits TOF distributions that are slower than MB at high θ_f for T_{liq} (Fig. 2(b), upper traces). The distribution at $\theta_f = 90°$ deviates significantly and we are not able to fit it with a single MB distribution. The same observation occurs in the cylindrical jet data (lower trace). Note that using a single SS distribution to fit the cylindrical jet TOF data would result in $T_{SS} = 217$ K and $v_{SS} = 0$ m s^{-1}, which is unrealistic as it would imply that the dramatic decrease in temperature is not accompanied by an increase in average flow velocity. Additionally, due to the low cross section of Ne-dodecane, it is unlikely that the distortion of the TOF distribution is caused by vapor collisions. We found that a linear combination of two Maxwellian distributions at T_{liq} (blue trace) and $T_{bkg} = 137$ K (light blue trace) best fits the data. The additional contribution is attributed to Ne evaporating from the cryogenically cooled copper walls, which we measured as 150 K using a thermocouple. The gradual broadening towards longer arrival times in the Ne TOF spectra for increasing θ_f is thus an artifact of a

constant cold Ne background which contributes more to the total signal as the intensity of Ne evaporating from the jet decreases (owing to the $\cos\theta_f$ distribution). Other possibilities leading to the additional spectral contribution, such as dodecane fragments or doubly-ionized residual argon background, have been systematically addressed and discarded. We observe this effect only for Ne as it is able to escape the cryogenically cooled surface.[70]

To further investigate the origin of the evaporating molecules, we integrate the TOF spectra and plot total intensity as a function of θ_f to yield the angular distributions presented in Fig. 3(b) for dodecane (red squares) and Ne (blue circles). The dodecane data shows that the total number of molecules evaporating from a flat surface follows the expected $\cos\theta_f$ distribution,[66, 71, 72] highlighting the unique ability of our experiment to measure accurate angular distributions of evaporating volatile liquids.

For Ne evaporation, the two Maxwellian contributions have been integrated separately. Since the TOF spectra in Fig. 2(b) were fit by assuming a homogeneous Ne background at T_{bkg} in the chamber, this component contributes a constant intensity at all angles (light blue triangles) in Fig. 3(b). The background-adjusted Ne component (the component at T_{liq}, blue circles) again follows $\cos\theta_f$, which further confirms that atoms and molecules with smaller van der Waals radii can escape the dodecane vapor region without undergoing enough gas-phase collisions to significantly distort their angular and velocity

distributions. These results suggest that Ne scattering experiments may also be largely unaffected by beam-vapor collisions, a point that will be explored in the next section. The slightly super-Maxwellian TOF distribution shape at 0˚ and the slightly narrowed cosine angular distribution could, however, reflect the interaction potential between Ne and dodecane.[65, 73]

3.2 Scattering

Fig. 5 shows TOF spectra from scattering of a fast Ne beam from flat (solid circles) and cylindrical (open circles) dodecane jets. In both cases, the detector is positioned at 90˚ with respect to the Ne beam. For a cylindrical jet, this corresponds to mean scattering angles of $\theta_i = 33^\circ \pm 22^\circ$ and $\theta_f = 57^\circ \pm 22^\circ$ with the uncertainty due to geometric effects.[60] To achieve a direct comparison to the cylindrical jet, the flat jet is rotated to $\theta_i = 33^\circ$, and the flat surface results in negligible variation in θ_i.. Data acquisition times for the two spectra were the same (~13 min). The S/N ratio from the flat jet is higher by a factor of 4.4; this represents a ~20-fold improvement of acquisition time t as S/N scales with $\sqrt{t}$. The TOF spectra are fit with a linear combination of SS and MB distributions representing IS and TD scattering channels, respectively.[74, 75] The same SS parameters fit both spectra regardless of the jet type, similar to what was seen for argon scattering off a liquid squalane ($P_{vap} = 10^{-7}$ Torr at 295 K) cylindrical jet and a wetted wheel,[37] indicating that the measured flat jet scattering signal reflects the interaction between the molecular beam and the liquid surface, rather than with the surrounding vapor sheath.

Our data shows a substantial amount of TD for Ne-dodecane scattering as compared to the data in ref. 37. A probable explanation is that our molecular beam was comparably slow with smaller translational energies (6.3 and 21.2 vs 50 kJ mol^{-1}) which increases the energy loss of the incident Ne atom (as we explore later in detail); thus, the probability of momentarily trapping the incoming gas molecules increases as the gas-surface interaction potential becomes more relevant for small translational energies.

Next, we scattered slow and fast Ne atoms impinging with $\theta_i = 60^\circ$ on a 278 K dodecane flat jet, shown in Fig. 6 for detector angles corresponding to $\theta_f = 30^\circ$, 50°, 70° and 90°. The molecular beam TOF spectra of the slow and fast beams are shown at the bottom of the two panels. Note that in contrast to the evaporation studies, a chopper wheel is not used in the scattering studies.

For both Ne beam energies, the scattered TOF spectra vary with θ_f; they become narrower and shift toward faster arrival times as θ_f increases, reflecting a diminished slow component contribution at larger angles. This trend is consistent with the expectation that TD produces a $\cos\theta_f$ distribution as was seen in our evaporation data. In fact, by using a two-component fit where a MB and a SS distribution are used for the slow and the fast portions of the TOF spectra, respectively, we can readily identify the slower scattered flux arising from TD and the faster scattered flux arising from IS. Note that this fitting procedure involves

convolution with the molecular beam temporal profile. As a general trend we observe a higher IS/TD ratio for the faster Ne beam, meaning fewer atoms become trapped at the liquid surface.

In order to further characterize these two channels, we plot in Fig. 7 the angular dependencies of the integrated TD and IS fits for the slow and fast Ne beams. As expected, the TD components follow a cosine angular distribution while the IS components are peaked around the 60˚ specular scattering angle. The fact that the TD contributions closely follow a cosine distribution in all cases indicates at least nearly complete thermal equilibration of the trapped atoms with the liquid surface.

We also carried out fast Ne scattering at incident angles of 45˚ and 80˚, shown in Fig. 8 and with contributions from the IS and TD components indicated. The overall trends remain similar, with the spectra narrowing as θ_f increases. The integrated intensities as a function of scattering angle shown in Fig. 9 demonstrate again that the TD component is best approximated by a cosine angular distribution while the IS component follows a narrow distribution peaked at the specular angle. Moreover, the IS component is clearly larger at the more grazing incidence angle $\theta_i = 80°$.

The observed trends of increasing IS/TD ratios with increasing θ_f and incident energy agree with existing literature.[76] These results reflect a higher trapping probability of Ne at the jet surface for smaller collision energies as the gas-surface interaction potential and thermal motion of the surface become more

relevant, and sufficient incident energy loss leads to Ne atoms being trapped at the surface. On the other hand, higher energy particles can escape the surface potential energy well more easily. Those trapped particles may then undergo thermal equilibration with the liquid and eventually evaporate, leading to an increased TD signal.

We next investigate the change in translational energy of the incident Ne beam by analyzing the IS component of the TOF spectra. The average fractional energy loss in the impulsive channel can be described as a function of deflection angle according to the "soft-sphere" kinematic model: [26, 77, 78]

$$\left(\frac{\Delta E}{E_i}\right) \approx \frac{2\mu}{(1+\mu)^2}\left[1+\mu(\sin\chi)^2-\cos\chi\sqrt{1-\mu^2(\sin\chi)^2-\frac{E_{int}}{E_i}(\mu+1)}+\frac{E_{int}}{E_i}\left(\frac{\mu+1}{2\mu}\right)\right]\left[1+\frac{V-2RT_{liq}}{E_i}\right] \quad (4)$$

with absolute change in translational energy $\Delta E = E_i$ - $\langle E_{IS}\rangle$, incident translational energy E_i, average energy in the IS channel $\langle E_{IS}\rangle$, mass ratio $\mu = m_{gas}/m_{eff}$ of the gas molecule and the effective surface mass, deflection angle $\chi = 180^\circ$ - ($\theta_i + \theta_f$), total internal excitation E_{int}, liquid temperature T_{liq}, and gas-surface interaction potential V. It should be noted that due to Ne having no internal degrees of freedom, E_{int} only applies to the liquid. This model has been successfully applied to both gas-solid[79] and gas-liquid[77] scattering studies.

Fig. 10 plots the calculated translational energy loss as a function of deflection angle for slow and fast Ne. We observe that an increased energy loss occurs when atoms exit more perpendicular to the surface (large χ) and the fastest emerging atoms recoil at grazing exit angles (small χ). At $\theta_i = 60^\circ$, the energy loss increases from 10 to 45% between $\chi = 30^\circ$ and 90° for fast Ne. For slow Ne, the fractional energy loss is considerably less, ranging from 0 to 15% over the same range of deflection angles.

Further, Fig. 10 contains fittings of Eq. 4 to the data. While m_{eff} and E_{int} are free parameters, we approximate $V = 0$ due to the small interaction between Ne and dodecane.[78] For comparison, *ab initio* calculations of the intermolecular interaction between *n*-pentane(g) and Ne(g) estimate the well depth to be 1.34 kJ mol^{-1},[80] while it is around 11-times deeper for the *n*-pentane dimer (14.9 kJ mol^{-1}).[81] Residuals analysis was then carried out for outlier detection. For slow Ne, the data point at $\chi = 30^\circ$ and one of the data points at $\chi = 60^\circ$ have been identified as outliers ($p < 0.002$) and thus discarded. For fast Ne no outliers were determined on the basis of residuals analysis.

Our $\Delta E/E_i$ fitting results yield 62 and 58 amu for the effective surface mass and E_{int} values of 1.9 and 0 kJ mol^{-1} for fast and slow Ne, respectively. The comparable effective surface masses for slow and fast Ne indicate that the incident gas particles experience an akin "stiffness" of the liquid surface. Similar results have been observed for atomic oxygen scattering from a squalane surface.[77, 82] It should be noted

that both fitted m_{eff} are smaller than the dodecane molecular mass, indicating that only parts of a single dodecane molecule are contributing to the scattering during the collision.

The fit results in Fig. 10 also show that the soft-sphere model (solid lines) is the correct kinematic model in this case. Fitting the "hard-sphere" model with $E_{\text{int}} = 0$ in Eq. 4 provides significantly worse agreement with the fast Ne data, as is indicated by the dashed lines in the figure. This shows that a considerable portion of energy contained in the fast Ne beam is transferred into internal excitation of the liquid. We estimate that 9% of E_{i} is converted into E_{int} for fast Ne while for slow Ne nearly no incident energy is dissipated into liquid internal excitation, hence higher incident energy collisions result in higher fractional energy loss.

The kinematic model also provides an explanation for the comparison between cylindrical and flat jet TOF spectra in Fig. 5. When fitting the data with the usual two components, we see that the IS channel (red trace) is identical for both setups. This is predicted by the model as the energy loss in the IS channel depends only on χ, rather than independently on θ_{i} and θ_{f}. The TD component is larger for the flat jet than for the cylindrical jet at the same incident energy. This effect might arise because cylindrical jet scattering samples larger incident angles where the TD component is lower in magnitude than at $\theta_{\text{i}} = 33°$.[60]

4. CONCLUSIONS

In this work, a flat liquid jet was incorporated into a crossed molecular beam instrument in order to investigate evaporation and scattering at the gas-liquid interface. Compared to a cylindrical liquid jet, the flat jet offers a considerably larger target area for scattering experiments and the ability to measure well-defined product angular distributions in evaporation and scattering studies. Here, we have reported results on the evaporation of dodecane and Ne from Ne-doped dodecane jets, and the scattering of Ne from pure dodecane jets.

In the evaporation experiments, both dodecane and Ne exhibit cosine angular distributions characteristic of thermal desorption. Time-of-flight measurements show that the dodecane translational energy distributions are "super-Maxwellian" at smaller scattering angles (near the surface normal) and become more "Maxwellian" at larger angles. This effect is attributed to scattering between evaporating molecules, analogous to what happens during a supersonic expansion. Ne atoms evaporating from the same dodecane surface are fit well by a Maxwell-Boltzmann distribution at all angles once the effects of background scattering from the cryo-cooled chamber walls are accounted for.

Scattering experiments from the surface of dodecane jets were carried out with fast and slow Ne beams. The combination of time-of-flight and angular distributions shows that the scattering could be fit with two

components, a faster impulsive scattering (IS) component whose angular distribution peaks at the specular angle, and a slower thermal desorption (TD) component that exhibits a cosine angular distribution. The scattering signals are substantially higher than those from a cylindrical jet under similar conditions, while the translational energy distributions of the two components are the same. The latter result indicates that the translational energy distributions from the flat jet reflect gas-liquid interactions rather than collisions with the vapor surrounding the flat jet. We find that the fast Ne scattering experiments exhibit more IS than TD scattering, consistent with previous work, and that the IS translational energy distributions show energy transfer to the liquid consistent with a "soft-sphere" kinematic model.

Future experiments will focus on more complex scattering partners and more volatile solvents. We are particularly interested in carrying out evaporation and scattering experiments on flat water jets in order to probe this very important gas-liquid interface and to sort out the effects expected from the increased vapor density surrounding such a jet. These experiments are currently in progress and will be reported soon.

AUTHOR INFORMATION

Corresponding Author

Daniel M. Neumark – *Department of Chemistry, University of California, Berkeley, CA 94720, USA*; *Chemical Sciences Division, Lawrence Berkeley National Laboratory, Berkeley, CA 94720, USA*; orcid.org/0000-0002-3762-9473; Email: dneumark@berkeley.edu

Authors

Chin Lee – *Department of Chemistry, University of California, Berkeley, CA 94720, USA*; *Chemical Sciences Division, Lawrence Berkeley National Laboratory, Berkeley, CA 94720, USA*; orcid.org/0000-0001-9011-0526

Marvin N. Pohl – *Department of Chemistry, University of California, Berkeley, CA 94720, USA*; *Chemical Sciences Division, Lawrence Berkeley National Laboratory, Berkeley, CA 94720, USA*; orcid.org/0000-0002-1790-8440

Isaac A. Ramphal – *Department of Chemistry, University of California, Berkeley, CA 94720, USA*; *Chemical Sciences Division, Lawrence Berkeley National Laboratory, Berkeley, CA 94720, USA*; orcid.org/0000-0002-6102-2065

Walt Yang – *Department of Chemistry, University of California, Berkeley, CA 94720, USA*; *Chemical Sciences Division, Lawrence Berkeley National Laboratory, Berkeley, CA 94720, USA*; orcid.org/0000-0003-4296-3801

Bernd Winter – *Molecular Physics, Fritz-Haber-Institut der Max-Planck-Gesellschaft, Faradayweg 4-6, 14195 Berlin, Germany*; orcid.org/0000-0002-5597-8888

Bernd Abel – *Leibniz Institute of Surface Engineering (IOM), Department of Functional Surfaces, Permoserstrasse 15, 04318 Leipzig, Germany*; *University of Leipzig, Wilhelm-Ostwald-Institute for Physical and Theoretical Chemistry, Linnéstrasse 3, 04318 Leipzig, Germany*; orcid.org/0000-0001-6032-1680

Author Contributions

‡These authors contributed equally.

ACKNOWLEDGMENTS

CL, MNP, IAR, WY and DMN acknowledge the support by the Office of Basic Energy Science, Chemical Sciences Division of the U.S. Department of Energy under Contract No. DE-AC02-05CH11231. CL, MNP, IAR, WY and DMN thank Daniel P. DePonte for useful

discussions regarding the chip design. MNP acknowledges additional support from the Alexander von Humboldt Foundation. BW acknowledges support from the German Research Foundation (Wi 1327/5-1). BA thanks the Miller Institute of the UC Berkeley for support through the Somorjai-Miller-Guest-Professorship Award, and the German Research Foundation for funding (AB63/19-1). This research used the resources of SLAC National Accelerator Laboratory, supported by the U.S. Department of Energy, Office of Science, Office of Basic Energy Sciences under Contract No. DE-AC02-76SF00515.

REFERENCES

1. Wallington, T. J.; Kaiser, E. W.; Farrell, J. T., Automotive fuels and internal combustion engines: a chemical perspective. *Chem. Soc. Rev.* **2006**, *35*, 335-347.
2. Singh, A.; Agrawal, M., Acid rain and its ecological consequences. *J. Environ. Biol.* **2008**, *29*, 15-24.
3. Putikam, R.; Lin, M. C., A novel mechanism for the isomerization of N_2O_4 and its implication for the reaction with H_2O and acid rain formation. *Int. J. Quantum Chem.* **2018**, *118*, e25560.
4. Ruiz-Lopez, M. F.; Martins-Costa, M. T. C.; Anglada, J. M.; Francisco, J. S., A New Mechanism of Acid Rain Generation from HOSO at the Air-Water Interface. *J. Am. Chem. Soc.* **2019**, *141*, 16564-16568.
5. Valsaraj, K. T., A Review of the Aqueous Aerosol Surface Chemistry in the Atmospheric Context. *Open J. Phys. Chem.* **2012**, *2*, 58-66.
6. Sabine, C. L.; Feely, R. A.; Gruber, N.; Key, R. M.; Lee, K.; Bullister, J. L.; Wanninkhof, R.; Wong, C. S.; Wallace, D. W. R.; Tilbrook, B.; Millero, F. J.; Peng, T. H.; Kozyr, A.; Ono, T.; Rios, A. F., The Oceanic Sink for Anthropogenic CO_2. *Science* **2004**, *305*, 367-371.
7. Finlayson-Pitts, B. J.; Pitts, J. N., *Chemistry of the Upper and Lower Atmosphere: Theory, Experiments, and Applications*. Academic Press: San Diego, 2000.
8. Jungwirth, P.; Tobias, D. J., Specific Ion Effects at the Air/Water Interface. *Chem. Rev.* **2006**, *106*, 1259-1281.
9. Ahmed, M.; Blum, M.; Crumlin, E. J.; Geissler, P. L.; Head-Gordon, T.; Limmer, D. T.; Mandadapu, K. K.; Saykally, R. J.; Wilson, K. R., Molecular Properties and Chemical Transformations Near Interfaces. *J. Phys. Chem. B* **2021**, *125*, 9037-9051.
10. Richmond, G. L., Molecular Bonding and Interactions at Aqueous Surfaces as Probed by Vibrational Sum Frequency Spectroscopy. *Chem. Rev.* **2002**, *102*, 2693-2724.
11. McGuire, J. A.; Shen, Y. R., Ultrafast Vibrational Dynamics at Water Interfaces. *Science* **2006**, *313*, 1945-1948.
12. Petersen, P. B.; Saykally, R. J., On the nature of ions at the liquid water surface. *Annu. Rev. Phys. Chem.* **2006**, *57*, 333-364.
13. Thurmer, S.; Seidel, R.; Faubel, M.; Eberhardt, W.; Hemminger, J. C.; Bradforth, S. E.; Winter, B., Photoelectron Angular Distributions from Liquid Water: Effects of Electron Scattering. *Phys. Rev. Lett.* **2013**, *111*, 173005.
14. Suzuki, Y. I.; Nishizawa, K.; Kurahashi, N.; Suzuki, T., Effective attenuation length of an electron in liquid water between 10 and 600 eV. *Phys. Rev. E* **2014**, *90*, 010302.
15. Signorell, R., Electron Scattering in Liquid Water and Amorphous Ice: A Striking Resemblance. *Phys. Rev. Lett.* **2020**, *124*, 205501.
16. Artiglia, L.; Edebeli, J.; Orlando, F.; Chen, S. Z.; Lee, M. T.; Arroyo, P. C.; Gilgen, A.; Bartels-Rausch, T.; Kleibert, A.; Vazdar, M.; Carignano, M. A.; Francisco, J. S.; Shepson, P. B.; Gladich, I.; Ammann, M., A surface-stabilized ozonide triggers bromide oxidation at the aqueous solution-vapour interface. *Nat. Commun.* **2017**, *8*, 700.
17. Ghosal, S.; Hemminger, J. C.; Bluhm, H.; Mun, B. S.; Hebenstreit, E. L. D.; Ketteler, G.; Ogletree, D. F.; Requejo, F. G.; Salmeron, M., Electron Spectroscopy of Aqueous Solution Interfaces Reveals Surface Enhancement of Halides. *Science* **2005**, *307*, 563-566.
18. Kappes, K. J.; Deal, A. M.; Jespersen, M. F.; Blair, S. L.; Doussin, J. F.; Cazaunau, M.; Pangui, E.; Hopper, B. N.; Johnson, M. S.; Vaida, V., Chemistry and Photochemistry of Pyruvic Acid at the Air-Water Interface. *J. Phys. Chem. A* **2021**, *125*, 1036-1049.
19. Li, Y. F.; Yan, X.; Cooks, R. G., The Role of the Interface in Thin Film and Droplet Accelerated Reactions Studied by Competitive Substituent Effects. *Angew. Chem. Int. Ed.* **2016**, *55*, 3433-3437.
20. Nam, I.; Lee, J. K.; Nam, H. G.; Zare, R. N., Abiotic production of sugar phosphates and uridine ribonudeoside in aqueous microdroplets. *Proc. Natl. Acad. Sci. U.S.A.* **2017**, *114*, 12396-12400.
21. Diveky, M. E.; Gleichweit, M. J.; Roy, S.; Signorell, R., Shining New Light on the Kinetics of Water Uptake by Organic Aerosol Particles. *J. Phys. Chem. A* **2021**, *125*, 3528-3548.
22. Neumark, D. M.; Wodtke, A. M.; Robinson, G. N.; Hayden, C. C.; Lee, Y. T., Molecular beam studies of the $F+H_2$ reaction. *J. Chem. Phys.* **1985**, *82*, 3045-3066.
23. Continetti, R. E.; Balko, B. A.; Lee, Y. T., Crossed molecular beams study of the reaction $D+H_2 \rightarrow DH+H$ at collision energies of 0.53 and 1.01 eV. *J. Chem. Phys.* **1990**, *93*, 5719-5740.
24. Weinberg, W. H., Molecular beam scattering from solid surfaces. *Adv. Colloid Interface Sci.* **1975**, *4*, 301-347.
25. Cardillo, M. J., Molecular beam scattering from solid surfaces: He diffraction, hyperthermal scattering, and surface dynamics. *Surf. Sci.* **1994**, *299*, 277-283.
26. Nathanson, G. M., Molecular beam studies of gas-liquid interfaces. *Annu. Rev. Phys. Chem.* **2004**, *55*, 231-255.

27. Kinefuchi, I.; Yamaguchi, H.; Shiozaki, S.; Sakiyama, Y.; Matsumoto, Y., Out-of-plane Scattering Distribution of Nitrogen Molecular Beam on Graphite (0001) Surface. *AIP Conf. Proc.* **2005**, *762*, 947-952.
28. Lednovich, S. L.; Fenn, J. B., Absolute Evaporation Rates for Some Polar and Nonpolar Liquids. *AIChE J.* **1977**, *23*, 454-459.
29. Siegbahn, H., Electron Spectroscopy for Chemical Analysis of Liquids and Solutions. *J. Phys. Chem.* **1985**, *89*, 897-909.
30. King, M. E.; Nathanson, G. M.; Hanninglee, M. A.; Minton, T. K., Probing the Microscopic Corrugation of Liquid Surfaces with Gas-Liquid Collisions. *Phys. Rev. Lett.* **1993**, *70*, 1026-1029.
31. Nathanson, G. M.; Davidovits, P.; Worsnop, D. R.; Kolb, C. E., Dynamics and Kinetics at the Gas-Liquid Interface. *J. Phys. Chem.* **1996**, *100*, 13007-13020.
32. Wu, B. H.; Zhang, J. M.; Minton, T. K.; McKendrick, K. G.; Slattery, J. M.; Yockel, S.; Schatz, G. C., Scattering Dynamics of Hyperthermal Oxygen Atoms on Ionic Liquid Surfaces: [emim][NTf_2] and [C_{12}mim][NTf_2]. *J. Phys. Chem. C* **2010**, *114*, 4015-4027.
33. Brastad, S. M.; Nathanson, G. M., Molecular beam studies of HCl dissolution and dissociation in cold salty water. *Phys. Chem. Chem. Phys.* **2011**, *13*, 8284-8295.
34. Lane, P. D.; Moncrieff, K. E.; Greaves, S. J.; McKendrick, K. G.; Costen, M. L., Inelastic Scattering of CN Radicals at the Gas-Liquid Interface Probed by Frequency-Modulated Absorption Spectroscopy. *J. Phys. Chem. C* **2020**, *124*, 16439-16448.
35. Faubel, M.; Schlemmer, S.; Toennies, J. P., A molecular beam study of the evaporation of water from a liquid jet. *Z. Phys. D: At., Mol. Clusters* **1988**, *10*, 269-277.
36. Faubel, M.; Kisters, T., Non-equilibrium molecular evaporation of carboxylic acid dimers. *Nature* **1989**, *339*, 527-529.
37. Lancaster, D. K.; Johnson, A. M.; Burden, D. K.; Wiens, J. P.; Nathanson, G. M., Inert Gas Scattering from Liquid Hydrocarbon Microjets. *J. Phys. Chem. Lett.* **2013**, *4*, 3045-3049.
38. Faust, J. A.; Sobyra, T. B.; Nathanson, G. M., Gas-Microjet Reactive Scattering: Collisions of HCl and DCl with Cool Salty Water. *J. Phys. Chem. Lett.* **2016**, *7*, 730-735.
39. Gord, J. R.; Zhao, X. Y.; Liu, E.; Bertram, T. H.; Nathanson, G. M., Control of Interfacial Cl_2 and N_2O_5 Reactivity by a Zwitterionic Phospholipid in Comparison with Ionic and Uncharged Surfactants. *J. Phys. Chem. A* **2018**, *122*, 6593-6604.
40. Shaloski, M. A.; Gord, J. R.; Staudt, S.; Quinn, S. L.; Bertram, T. H.; Nathanson, G. M., Reactions of N_2O_5 with Salty and Surfactant-Coated Glycerol: Interfacial Conversion of Br^- to Br_2 Mediated by Alkylammonium Cations. *J. Phys. Chem. A* **2017**, *121*, 3708-3719.
41. Sobyra, T. B.; Melvin, M. P.; Nathanson, G. M., Liquid Microjet Measurements of the Entry of Organic Acids and Bases into Salty Water. *J. Phys. Chem. C* **2017**, *121*, 20911-20924.
42. Ekimova, M.; Quevedo, W.; Faubel, M.; Wernet, P.; Nibbering, E. T. J., A liquid flatjet system for solution phase soft-x-ray spectroscopy. *Struct. Dyn.* **2015**, *2*, 054301.
43. Luu, T. T.; Yin, Z.; Jain, A.; Gaumnitz, T.; Pertot, Y.; Ma, J.; Worner, H. J., Extreme-ultraviolet high-harmonic generation in liquids. *Nat. Commun.* **2018**, *9*, 3723.
44. Menzi, S.; Knopp, G.; Al Haddad, A.; Augustin, S.; Borca, C.; Gashi, D.; Huthwelker, T.; James, D.; Jin, J.; Pamfilidis, G.; Schnorr, K.; Sun, Z. B.; Wetter, R.; Zhang, Q.; Cirelli, C., Generation and simple characterization of flat, liquid jets. *Rev. Sci. Instrum.* **2020**, *91*.
45. Tcypkin, A. N.; Ponomareva, E. A.; Putilin, S. E.; Smirnov, S. V.; Shtumpf, S. A.; Melnik, M. V.; Yiwen, E.; Kozlov, S. A.; Zhang, X. C., Flat liquid jet as a highly efficient source of terahertz radiation. *Opt. Express* **2019**, *27*, 15485-15494.
46. Malerz, S.; Haak, H.; Trinter, F.; Stephansen, A. B.; Kolbeck, C.; Pohl, M.; Hergenhahn, U.; Meijer, G.; Winter, B., A setup for studies of photoelectron circular dichroism from chiral molecules in aqueous solution. *Rev. Sci. Instrum.* **2022**, *93*, 015101.
47. Edwards, T.; Maurice, L. Q., Surrogate Mixtures to Represent Complex Aviation and Rocket Fuels. *J. Propul. Power* **2001**, *17*, 461-466.
48. Lee, Y. T.; Mcdonald, J. D.; Lebreton, P. R.; Herschbach, D. R., Molecular Beam Reactive Scattering Apparatus with Electron Bombardment Detector. *Rev. Sci. Instrum.* **1969**, *40*, 1402-1408.
49. Lee, Y. T., Molecular Beam Studies of Elementary Chemical Processes (Nobel Lecture). *Angew. Chem. Int. Ed.* **1987**, *26*, 939-951.
50. Irimia, D.; Dobrikov, D.; Kortekaas, R.; Voet, H.; van den Ende, D. A.; Groen, W. A.; Janssen, M. H. M., A short pulse (7 μs FWHM) and high repetition rate (dc-5kHz) cantilever piezovalve for pulsed atomic and molecular beams. *Rev. Sci. Instrum.* **2009**, *80*, 113303.

51. Meng, C. S.; Janssen, M. H. M., Measurement of the density profile of pure and seeded molecular beams by femtosecond ion imaging. *Rev. Sci. Instrum.* **2015**, *86*, 023110.
52. Umrath, W., *Fundamentals of Vacuum Technology*. Oerlikon Leybold Vacuum: Cologne, 2007.
53. Charvat, A.; Lugovoj, E.; Faubel, M.; Abel, B., New design for a time-of-flight mass spectrometer with a liquid beam laser desorption ion source for the analysis of biomolecules. *Rev. Sci. Instrum.* **2004**, *75*, 1209-1218.
54. Bush, J. W. M.; Hasha, A. E., On the collision of laminar jets: fluid chains and fishbones. *J. Fluid Mech.* **2004**, *511*, 285-310.
55. Bremond, N.; Villermaux, E., Atomization by jet impact. *J. Fluid Mech.* **2006**, *549*, 273-306.
56. Koralek, J. D.; Kim, J. B.; Bruza, P.; Curry, C. B.; Chen, Z. J.; Bechtel, H. A.; Cordones, A. A.; Sperling, P.; Toleikis, S.; Kern, J. F.; Moeller, S. P.; Glenzer, S. H.; DePonte, D. P., Generation and characterization of ultrathin free-flowing liquid sheets. *Nat. Commun.* **2018**, *9*, 1353.
57. Winter, B., Liquid microjet for photoelectron spectroscopy. *Nucl. Instrum. Meth. A* **2009**, *601*, 139-150.
58. NIST Mass Spectrometry Data Center, W. E. W., director, Mass Spectra. In *NIST Chemistry WebBook, NIST Standard Reference Database 69* [Online] Linstrom, P. J.; Mallard, W. G., Eds. NIST Mass Spectrometry Data Center, William E. Wallace, director: National Institute of Standards and Technology, Gaithersburg MD, 20899, 2014. https://doi.org/10.18434/T4D303 (accessed February 14, 2022).
59. Cappa, C. D.; Drisdell, W. S.; Smith, J. D.; Saykally, R. J.; Cohen, R. C., Isotope Fractionation of Water during Evaporation without Condensation. *J. Phys. Chem. B* **2005**, *109*, 24391-24400.
60. Faust, J. A.; Nathanson, G. M., Microjets and coated wheels: versatile tools for exploring collisions and reactions at gas-liquid interfaces. *Chem. Soc. Rev.* **2016**, *45*, 3609-3620.
61. Sasse, K.; Jose, J.; Merlin, J. C., A static apparatus for measurement of low vapor pressures. Experimental results on high molecular-weight hydrocarbons. *Fluid Phase Equilib.* **1988**, *42*, 287-304.
62. Comsa, G.; David, R., Dynamical parameters of desorbing molecules. *Surf. Sci. Rep.* **1985**, *5*, 145-198.
63. Lebehot, A.; Kurzyna, J.; Lago, V.; Dudeck, M.; Campargue, R., Laser Sustained Plasma Free Jet and Energetic Atom Beam of Pure Argon or Oxygen Seeded Argon Mixture. In *Atomic and Molecular Beams*, Campargue, R., Ed. Springer: New York, 2001; pp 267-251.
64. Morse, M. D., SUPERSONIC BEAM SOURCES. In *Atomic, Molecular, and Optical Physics: Atoms and Molecules*, Dunning, F. B.; Hulet, R. G., Eds. Academic Press: 1996; Vol. 29B, pp 21-47.
65. Kann, Z. R.; Skinner, J. L., Sub- and super-Maxwellian evaporation of simple gases from liquid water. *J. Chem. Phys.* **2016**, *144*, 154701.
66. Kennard, E. H., *Kinetic Theory of Gases*. 1 ed.; McGraw-Hill Book Company: New York, 1938.
67. Bochko, V.; Silagadze, Z. K., On the electrostatic potential and electric field of a uniformly charged disk. *Eur. J. Phys.* **2020**, *41*, 045201.
68. Purcell, E. M.; Morin, D. J., *Electricity and magnetism*. 3 ed.; Cambridge University Press: Cambridge, 2013.
69. Cummings, G. A. M.; Ubbelohde, A. R., Collision Diameters of Flexible Hydrocarbon Molecules in the Vapour Phase: The "Hydrogen Effect". *J. Chem. Soc.* **1953**, 3751-3755.
70. Day, C., Basics and applications of cryopumps. In *CAS - CERN Accelerator School : Vacuum in Accelerators*, 2007; pp 241-274.
71. Garton, D. J.; Minton, T. K.; Alagia, M.; Balucani, N.; Casavecchia, P.; Volpi, G. G., Comparative dynamics of Cl(^2P) and O(^3P) interactions with a hydrocarbon surface. *J. Chem. Phys.* **2000**, *112*, 5975-5984.
72. King, M. E.; Fiehrer, K. M.; Nathanson, G. M.; Minton, T. K., Effects of Thermal Roughening on the Angular Distributions of Trapping and Scattering in Gas-Liquid Collisions. *J. Phys. Chem. A* **1997**, *101*, 6556-6561.
73. Patel, E. H.; Williams, M. A.; Koehler, S. P. K., Kinetic Energy and Angular Distributions of He and Ar Atoms Evaporating from Liquid Dodecane. *J. Phys. Chem. B* **2017**, *121*, 233-239.
74. Saecker, M. E.; Govoni, S. T.; Kowalski, D. V.; King, M. E.; Nathanson, G. M., Molecular Beam Scattering from Liquid Surfaces. *Science* **1991**, *252*, 1421-1424.
75. Kinefuchi, I.; Kotsubo, Y.; Osuka, K.; Yoshimoto, Y.; Miyoshi, N.; Takagi, S.; Matsumoto, Y., Incident energy dependence of the scattering dynamics of water molecules on silicon and graphite surfaces: the effect on tangential momentum accommodation. *Microfluid. Nanofluidics* **2017**, *21*, 15.
76. Headgordon, M.; Tully, J. C.; Rettner, C. T.; Mullins, C. B.; Auerbach, D. J., On the nature of trapping and desorption at high surface temperatures. Theory and experiments for the Ar-Pt(111) system. *J. Chem. Phys.* **1991**, *94*, 1516-1527.
77. Alexander, W. A.; Zhang, J. M.; Murray, V. J.; Nathanson, G. M.; Minton, T. K., Kinematics and dynamics of atomic-beam scattering on liquid and self-assembled monolayer surfaces. *Faraday Discuss.* **2012**, *157*, 355-374.
78. Rettner, C. T.; Ashfold, M. N. R., In *Dynamics of Gas-Surface Interactions*, Royal Society of Chemistry: Cambridge, 1991.
79. Andric, N.; Jenny, P., Molecular dynamics investigation of energy transfer during gas-surface collisions. *Phys. Fluids* **2018**, *30*, 077104.

80. Balabin, R. M., Intermolecular dispersion interactions of normal alkanes with rare gas atoms: van der Waals complexes of *n*-pentane with helium, neon, and argon. *Chem. Phys.* **2008**, *352*, 267-275.
81. Tsuzuki, S.; Honda, K.; Uchimaru, T.; Mikami, M., Magnitude of Interaction between *n*-Alkane Chains and Its Anisotropy: High-Level ab Initio Calculations of *n*-Butane, *n*-Petane, and *n*-Hexane Dimers. *J. Phys. Chem. A* **2004**, *108*, 10311-10316.
82. Zhang, J. M.; Garton, D. J.; Minton, T. K., Reactive and inelastic scattering dynamics of hyperthermal oxygen atoms on a saturated hydrocarbon surface. *J. Chem. Phys.* **2002**, *117*, 6239-6251.

FIGURES

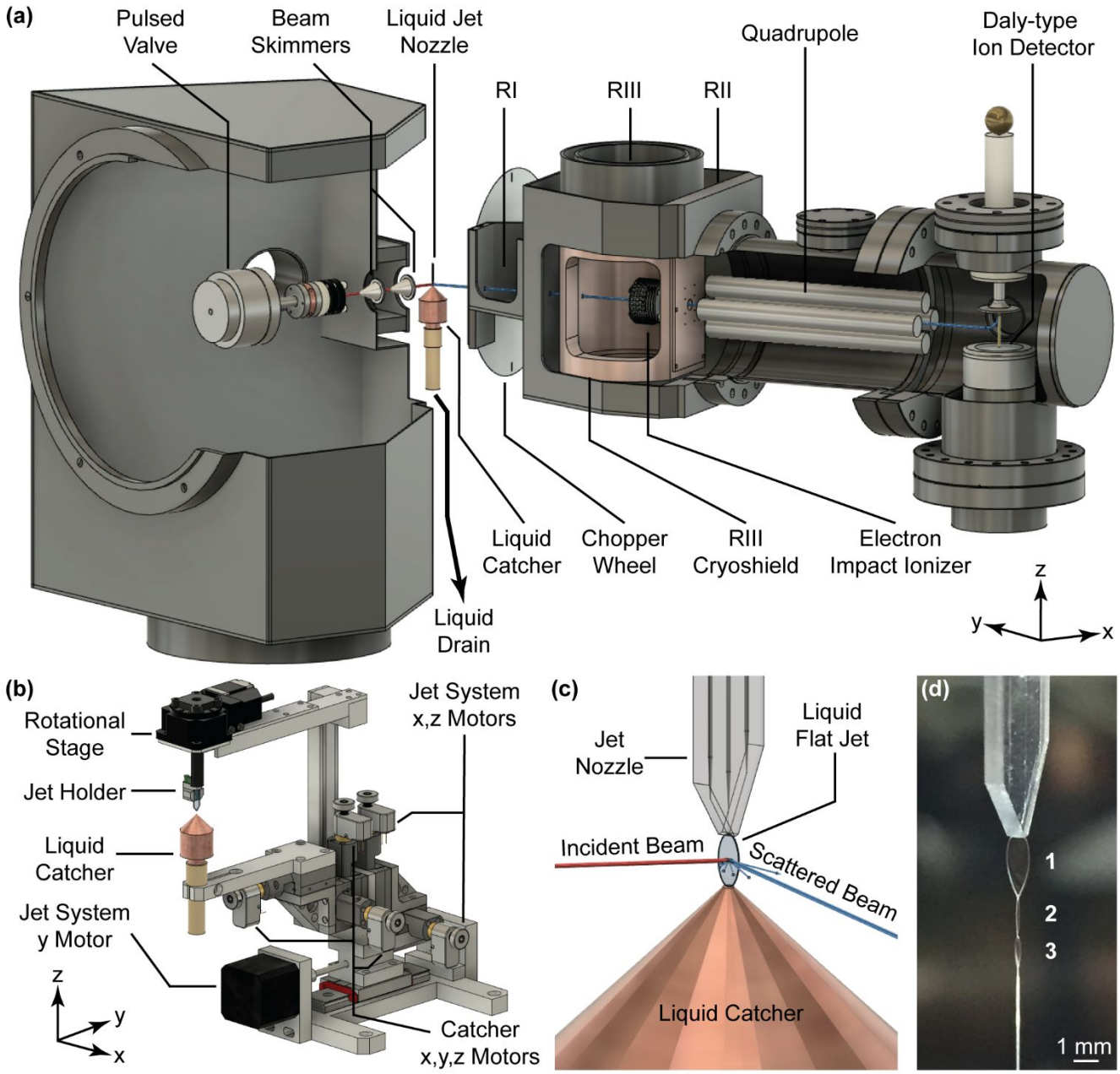

Figure 1. (a) Sectional view of our scattering apparatus with crucial components highlighted. All components are situated inside the main chamber (not shown). The chamber on the left housing the pulsed

valve is referred to as the source chamber, while the chamber on the right containing all detector components is referred to as the detector chamber. Lines indicate the molecular beam (red trace) striking the flat liquid jet surface and scattering off it (blue trace). Scattered molecules are then ionized, mass selected and subsequently collide onto a negatively charged high-voltage electrode. The generated secondary electrons (yellow trace) accelerate towards a scintillator, which emits photons that are collected and amplified by a photomultiplier tube. (b) 7-axis jet holder system. Details are given in the main text. (c) Zoomed-in view of the jet-catcher assembly. The liquid catcher is carefully positioned at the first jet node to reduce the main chamber pressure. (d) Photograph of a stable dodecane flat jet at 2.5 mL min^{-1} liquid flow rate, demonstrating formation of multiple perpendicular liquid sheets. Under optimal conditions, several perpendicular liquid sheets can be produced.

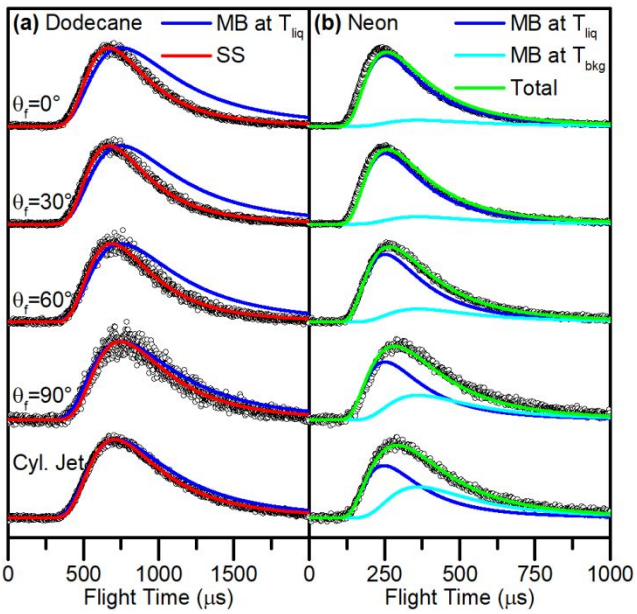

Figure 2. (a) Normalized evaporation TOF spectra of dodecane (detected at $m/z = 57$) from a Ne-doped liquid dodecane flat jet at 268 K and cylindrical jet at 289 K. TOF distributions are fit with a supersonic beam distribution (red traces). Maxwell-Boltzmann velocity distributions at the liquid temperature (blue traces) are shown for comparison. (b) Normalized evaporation TOF spectra of neon ($m/z = 20$) from a Ne-doped liquid dodecane flat jet at 283 K and cylindrical jet (bottom) at 291 K. Distributions are fit with a combination of Maxwell-Boltzmann velocity distributions at the liquid temperature (blue traces) and at $T_{bkg} = 137$ K (light blue traces). The absolute intensity of the T_{bkg} component has been kept constant for all angles. The sum of the two contributions is shown by the green traces.

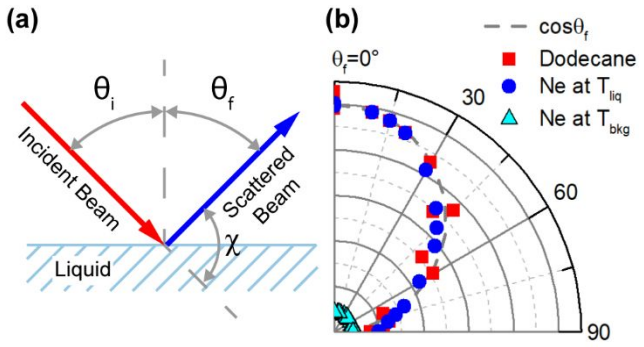

Figure 3. (a) Schematic plot of the scattering geometry. An incident beam (red arrow) is targeted onto the liquid surface (light blue section lines) at an incident angle θ_i. The scattered beam (blue arrow) is detected at the outgoing angle θ_f. (b) Angular plot created from the integrated, non-normalized intensities of the supersonic (red squares) and Maxwell-Boltzmann simulations at T_{liq} and T_{bkg} (blue circles and light blue triangles, respectively) of dodecane and Ne evaporation data at different angles. The cosine function representing the expected angular distribution for evaporation is indicated by the dashed, gray curve.

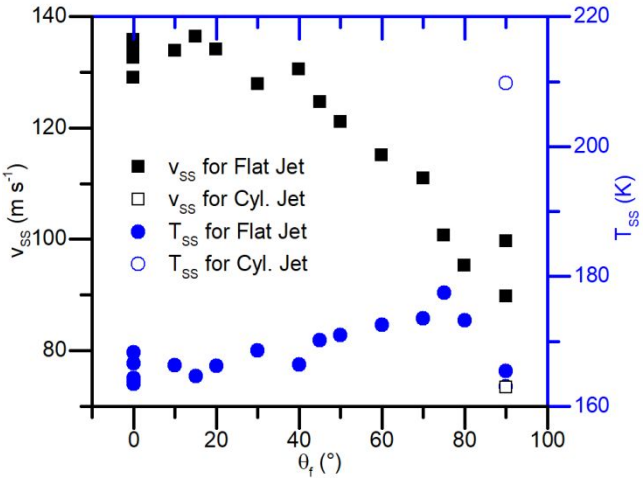

Figure 4. Supersonic beam fit parameters v_{SS} (black squares) and T_{SS} (blue circles) of the velocity distribution of the evaporating dodecane molecules from a flat (solid) and a cylindrical (open) jet at different detector angles θ_f. T_{liq} is 268 and 289 K for flat and cylindrical jets, respectively.

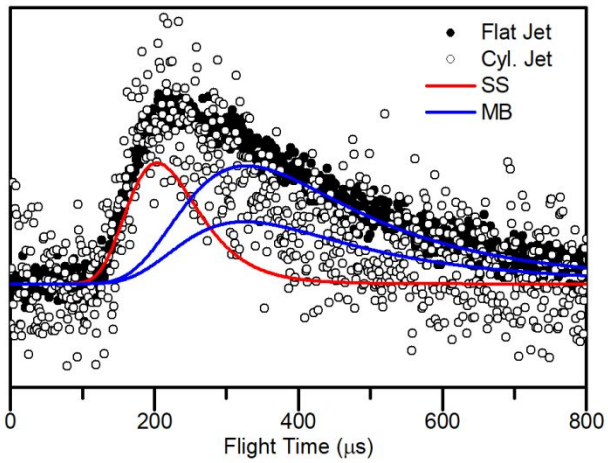

Figure 5. Normalized TOF spectra for scattering of fast Ne atoms from dodecane using a flat (solid circles) and a cylindrical (open circles) liquid jet. Solid lines show the simulations of the IS component (red trace, supersonic) and TD components (blue traces, Maxwellian at T_{liq} = 278 and 283 K for the flat and cylindrical jet, respectively).

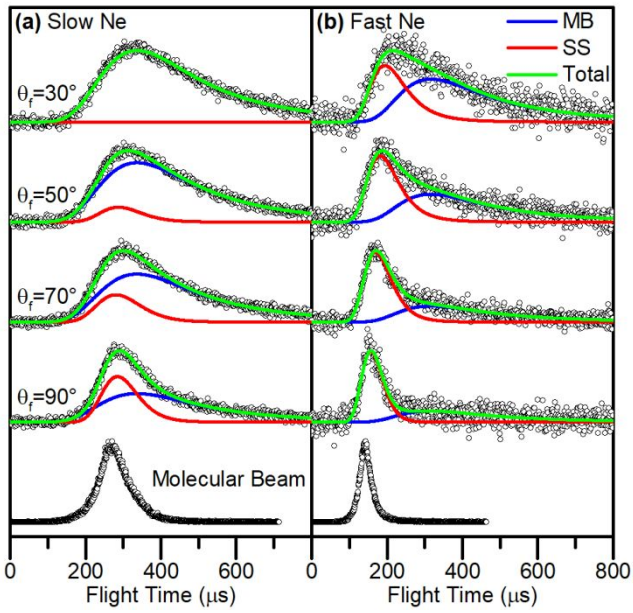

Figure 6. Normalized TOF spectra of (a) slow and (b) fast Ne scattering off a dodecane flat jet with $\theta_i = 60^\circ$. The data are fit by the sum of a SS distribution (red traces) and a MB distribution at the liquid jet temperature (278 K and 277 K for slow and fast Ne, blue traces). The sum of the two contributions is shown by the green traces. The normalized temporal profiles of the molecular beams are shown at the bottom for reference.

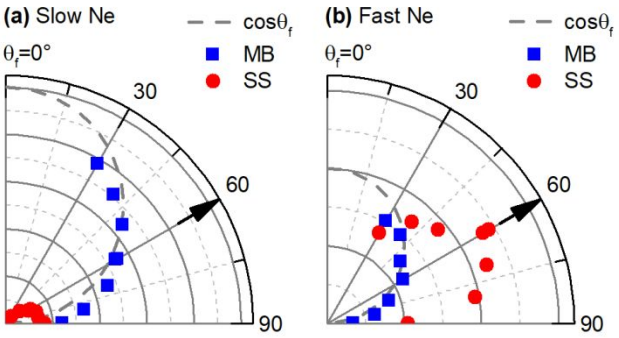

Figure 7. Angular plots created from the integrated, non-normalized intensities of the Ne scattering data at different angles for (a) slow and (b) fast Ne beams. Blue squares represent the TD and red circles the IS contributions to the TOF fits. The cosine function representing the expected angular distribution for evaporation is indicated by the dashed, gray line. Arrows indicate the specular angle.

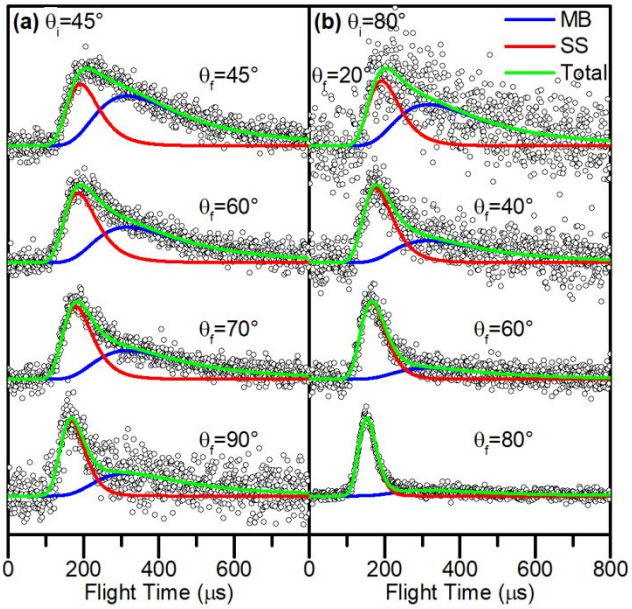

Figure 8. Normalized TOF spectra of fast neon scattering off a dodecane flat jet with (a) $\theta_i = 45^\circ$ and (b) $\theta_i = 80^\circ$ and collected by varying θ_f. The data are fit by the sum of a SS distribution (red traces) and a MB distribution (blue traces) at the liquid jet temperature (276 and 278 K for $\theta_i = 45^\circ$ and 80°, respectively). The total fits are shown by the green traces.

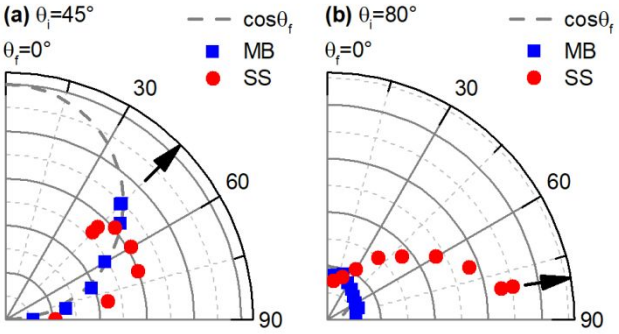

Figure 9. Angular plots created from the integrated, non-normalized intensities of the fast Ne scattering data at different angles for (a) $\theta_i = 45^\circ$ and (b) 80°. Blue squares represent the TD and red circles the IS contributions to the TOF fits. The cosine function representing the expected angular distribution for evaporation is indicated by the dashed, gray line. Arrows indicate the specular angle.

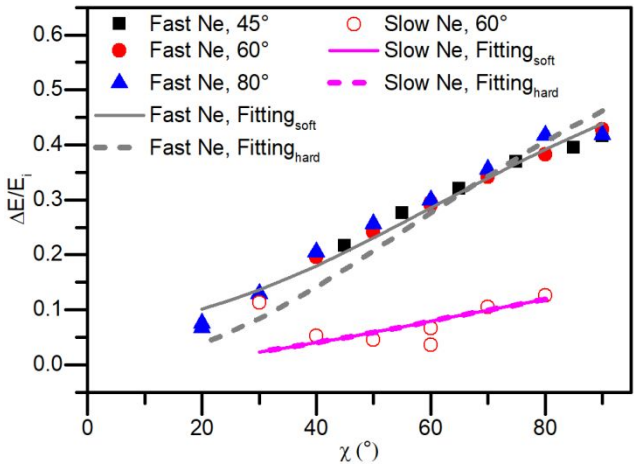

Figure 10. Average fractional energy loss as a function of deflection angle for impulsively scattered (IS) slow and fast Ne atoms from a dodecane flat jet. Incident translational energies are 6.3 and 21.2 kJ mol^{-1} for slow and fast Ne beams, respectively, and incident angles are indicated in the legend. The solid lines give the predictions of the soft-sphere model, where the incident atom interacts with a localized region of the surface with effective mass, m_{eff}, and this region may increase its internal energy, E_{int}, during collisions. The dashed lines are the predictions of the hard-sphere model where internal excitation has been set to zero. For the slow beam the soft-sphere and hard-sphere models give indistinguishable predictions. The fitting results for fast and slow Ne with the soft-sphere model are m_{eff} = 62 and 58 amu, and E_{int} = 1.9 and 0 kJ mol^{-1}, respectively, whereas the hard-sphere model predicts m_{eff} = 48 and 58 amu, respectively.

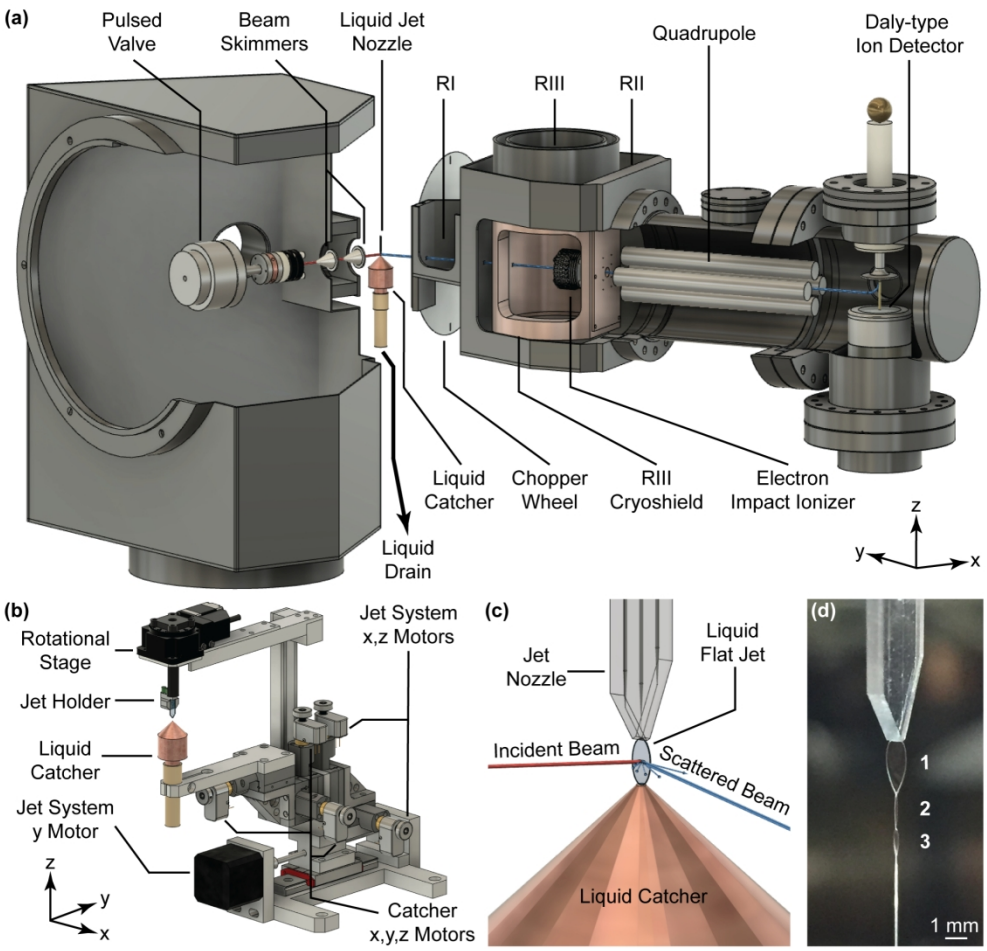

(a) Sectional view of our scattering apparatus with crucial components highlighted. All components are situated inside the main chamber (not shown). The chamber on the left housing the pulsed valve is referred to as the source chamber, while the chamber on the right containing all detector components is referred to as the detector chamber. Lines indicate the molecular beam (red trace) striking the flat liquid jet surface and scattering off it (blue trace). Scattered molecules are then ionized, mass selected and subsequently collide onto a negatively charged high voltage electrode. The generated secondary electrons (yellow trace) accelerate towards a scintillator, which emits photons that are collected and amplified by a photomultiplier tube. (b) 7 axis jet holder system. Details are given in the main text. (c) Zoomed in view of the jet catcher assembly. The liquid catcher is carefully positioned at the first jet node to reduce the main chamber pressure. (d) Photograph of a stable dodecane flat jet at 2.5 mL min-1 liquid flow rate, demonstrating formation of multiple perpendicular liquid sheets. Under optimal conditions, several perpendicular liquid sheets can be produced.

741x709mm (72 x 72 DPI)

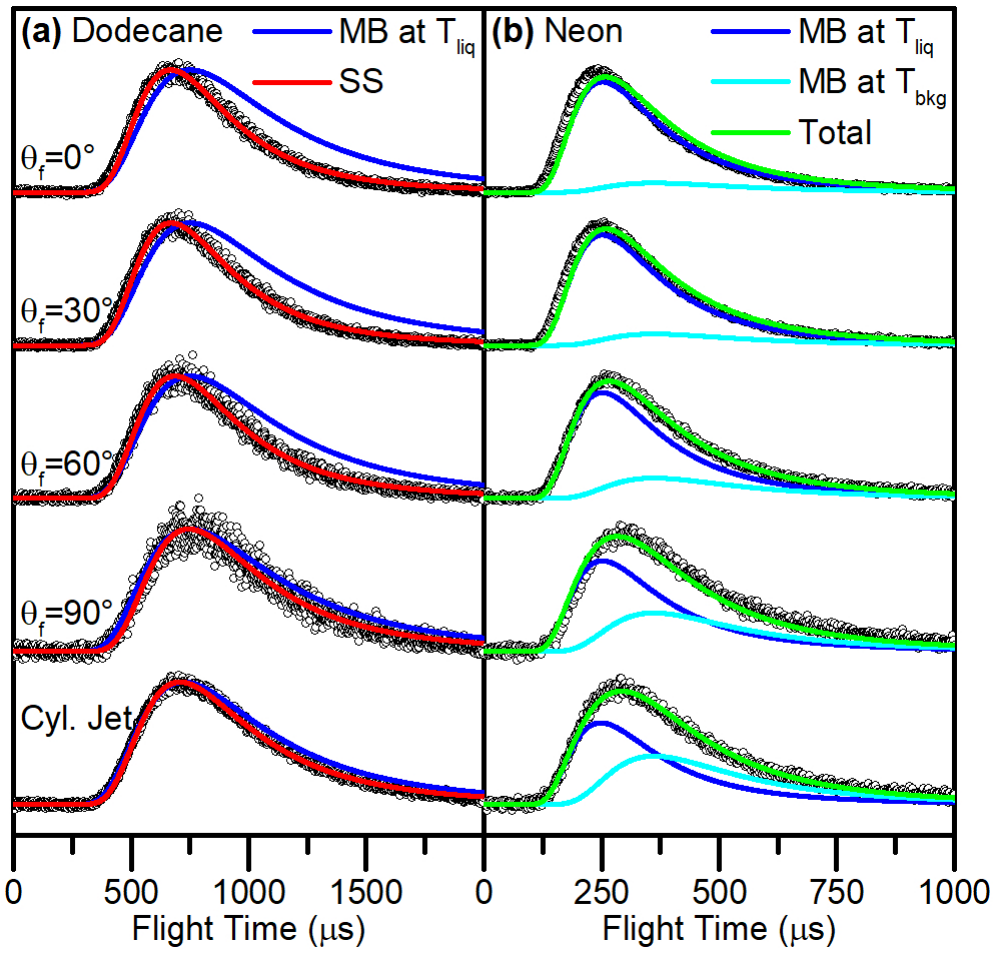

(a) Normalized evaporation TOF spectra of dodecane (detected at m/z = 57) from a Ne doped liquid dodecane flat jet at 268 K and cylindrical jet at 289 K. TOF distributions are fit with a supersonic beam distribution (red traces). Maxwell Boltzmann velocity distributions at the liquid temperature (blue traces) are shown for comparison. (b) Normalized evaporation TOF spectra of neon (m/z = 20) from a Ne doped liquid dodecane flat jet at 283 K and cylindrical jet (bottom) at 291 K. Distributions are fit with a combination of Maxwell Boltzmann velocity distributions at the liquid temperature (blue traces) and at Tbkg = 137 K (light blue traces). The absolute intensity of the Tbkg component has been kept constant for all angles. The sum of the two contributions is shown by the green traces.

84x81mm (300 x 300 DPI)

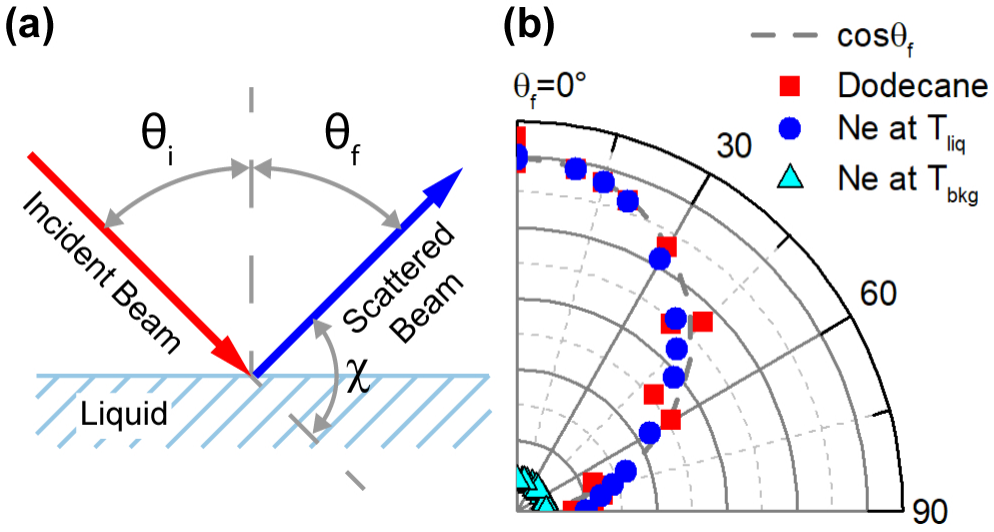

(a) Schematic plot of the scattering geometry. An incident beam (red arrow) is targeted onto the liquid surface (light blue section lines) at an incident angle θi. The scattered beam (blue arrow) is detected at the outgoing angle θf. (b) Angular plot created from the integrated, non-normalized intensities of the supersonic (red squares) and Maxwell-Boltzmann simulations at Tliq and Tbkg (blue circles and light blue triangles, respectively) of dodecane and Ne evaporation data at different angles. The cosine function representing the expected angular distribution for evaporation is indicated by the dashed, gray curve.

352x192mm (72 x 72 DPI)

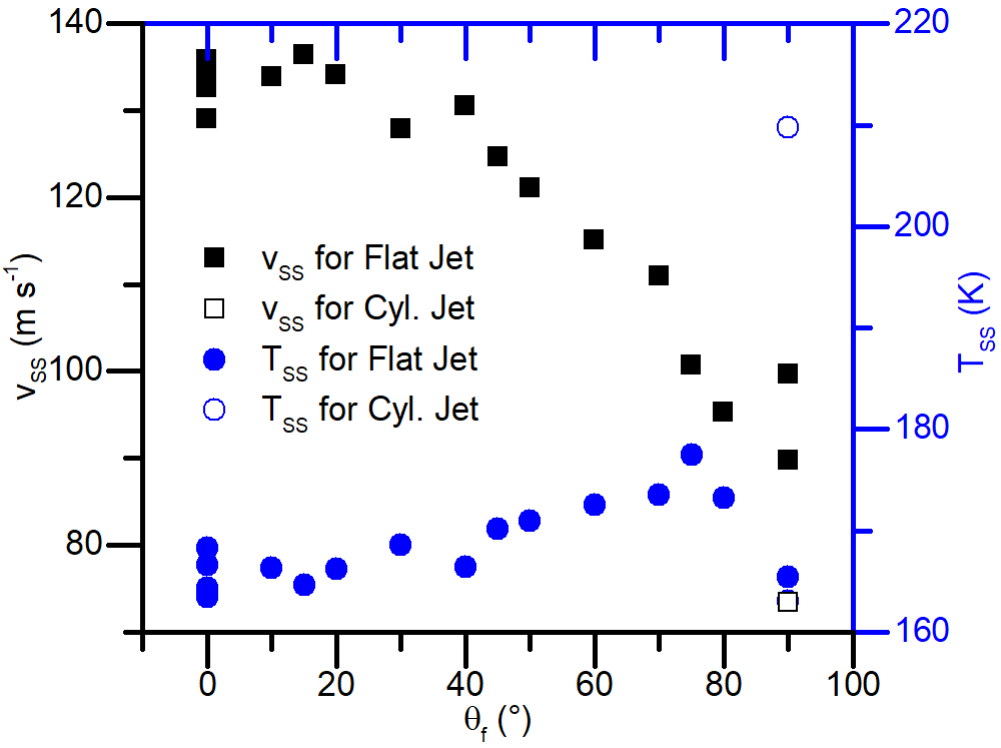

Supersonic beam fit parameters vSS (black squares) and TSS (blue circles) of the velocity distribution of the evaporating dodecane molecules from a flat (solid) and a cylindrical (open) jet at different detector angles θf. Tliq is 268 and 289 K for flat and cylindrical jets, respectively.

84x63mm (300 x 300 DPI)

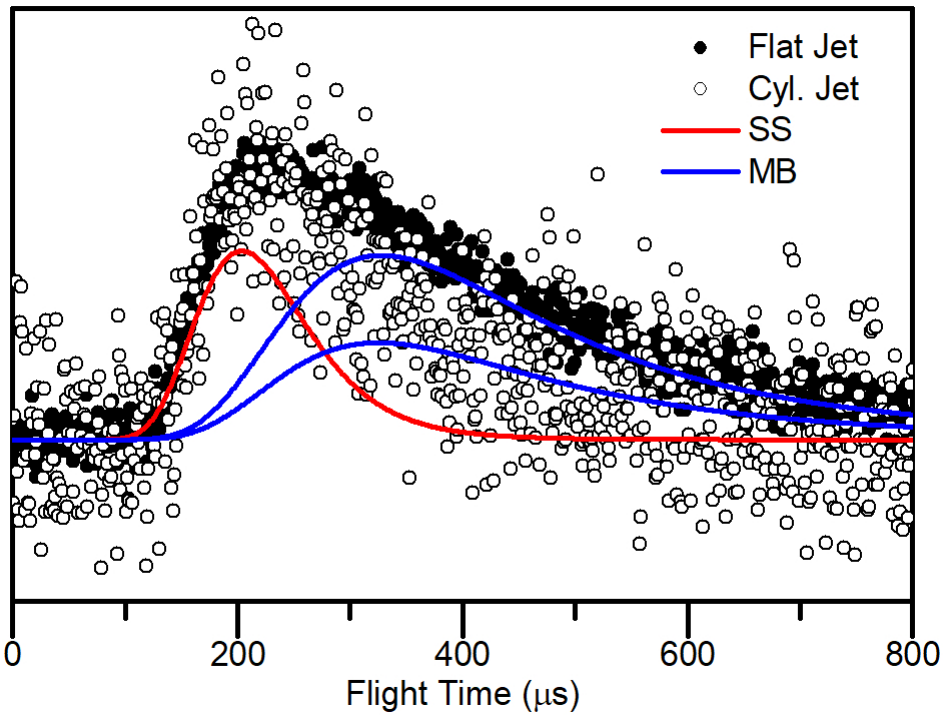

Normalized TOF spectra for scattering of fast Ne atoms from dodecane using a flat (solid circles) and a cylindrical (open circles) liquid jet. Solid lines show the simulations of the IS component (red trace, supersonic) and TD components (blue traces, Maxwellian at Tliq = 278 and 283 K for the flat and cylindrical jet, respectively).

84x63mm (300 x 300 DPI)

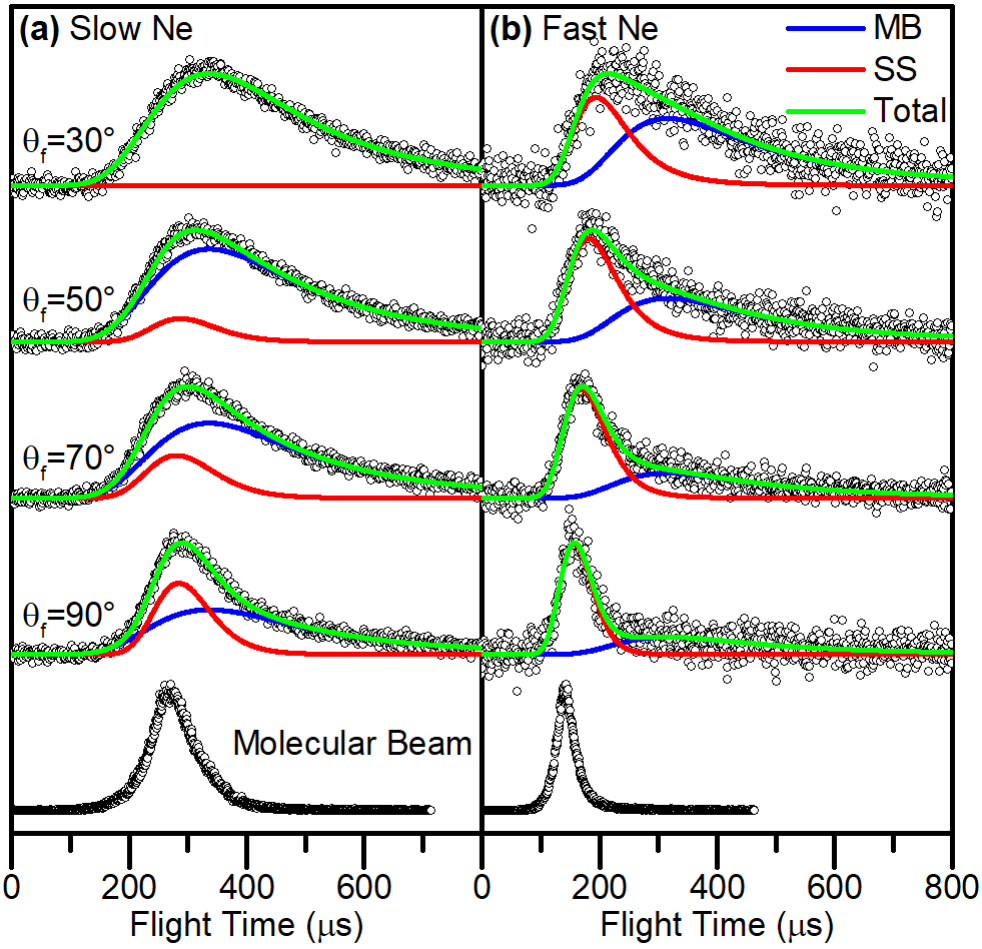

Normalized TOF spectra of (a) slow and (b) fast Ne scattering off a dodecane flat jet with θi = 60°. The data are fit by the sum of a SS distribution (red traces) and a MB distribution at the liquid jet temperature (278 K and 277 K for slow and fast Ne, blue traces). The sum of the two contributions is shown by the green traces. The normalized temporal profiles of the molecular beams are shown at the bottom for reference.

84x81mm (300 x 300 DPI)

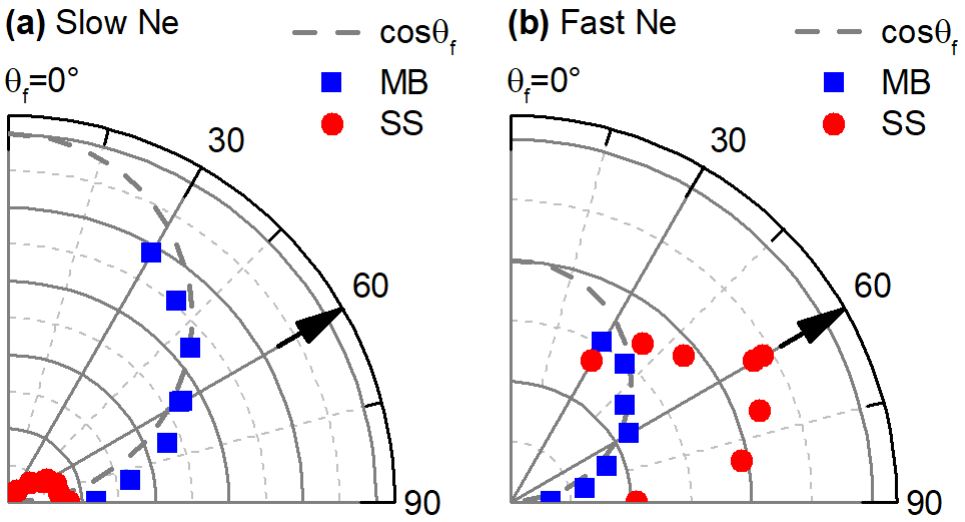

Angular plots created from the integrated, non-normalized intensities of the Ne scattering data at different angles for (a) slow and (b) fast Ne beams. Blue squares represent the TD and red circles the IS contributions to the TOF fits. The cosine function representing the expected angular distribution for evaporation is indicated by the dashed, gray line. Arrows indicate the specular angle.

84x45mm (300 x 300 DPI)

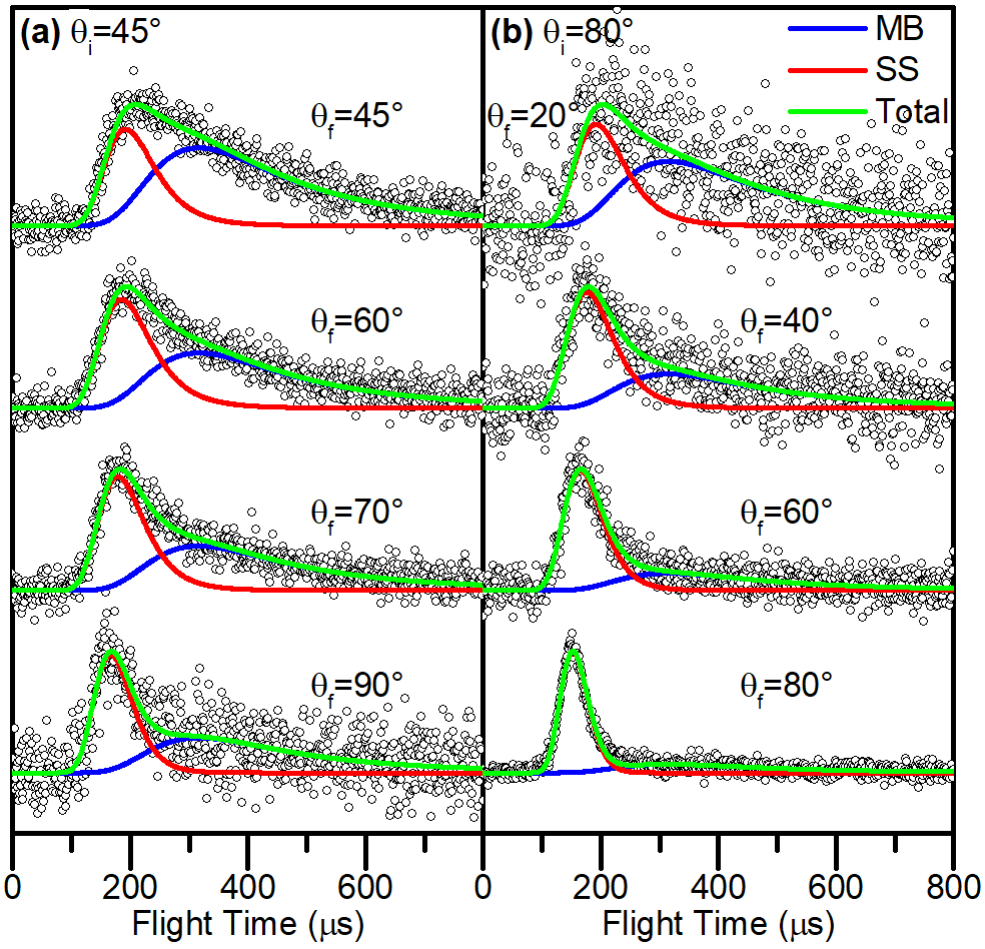

Normalized TOF spectra of fast neon scattering off a dodecane flat jet with (a) θi = 45° and (b) θi = 80° and collected by varying θf. The data are fit by the sum of a SS distribution (red traces) and a MB distribution (blue traces) at the liquid jet temperature (276 and 278 K for θi = 45° and 80°, respectively). The total fits are shown by the green traces.

84x81mm (300 x 300 DPI)

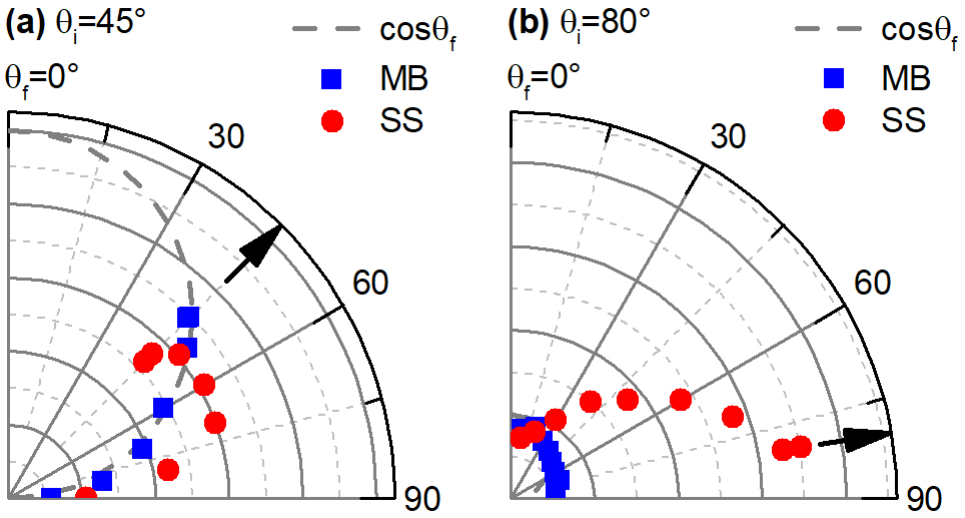

Angular plots created from the integrated, non normalized intensities of the fast Ne scattering data at different angles for (a) θi = 45° and (b) 80°. Blue squares represent the TD and red circles the IS contributions to the TOF fits. The cosine function representing the expected angular distribution for evaporation is indicated by the dashed, gray line. Arrows indicate the specular angle.

84x45mm (300 x 300 DPI)

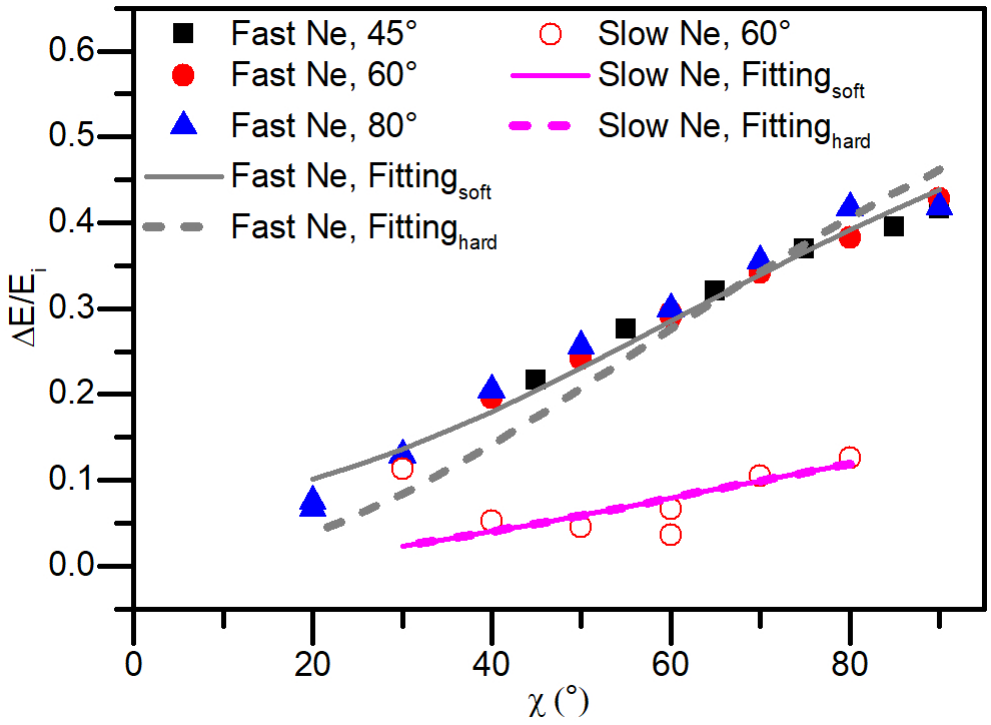

Average fractional energy loss as a function of deflection angle for impulsively scattered (IS) slow and fast Ne atoms from a dodecane flat jet. Incident translational energies are 6.3 and 21.2 kJ mol 1 for slow and fast Ne beams, respectively, and incident angles are indicated in the legend. The solid lines give the predictions of the soft sphere model, where the incident atom interacts with a localized region of the surface with effective mass, meff, and this region may increase its internal energy, Eint, during collisions. The dashed lines are the predictions of the hard sphere model where internal excitation has been set to zero. For the slow beam the soft sphere and hard sphere models give indistinguishable predictions. The fitting results for fast and slow Ne with the soft sphere model are meff = 62 and 58 amu, and Eint = 1.9 and 0 kJ mol-1, respectively, whereas the hard sphere model predicts meff = 48 and 58 amu, respectively.

84x63mm (300 x 300 DPI)